Journal of Magnetic Resonance Open 16–17 (2023) 100136

Contents lists available at ScienceDirect

Journal of Magnetic Resonance Open

journal homepage: www.sciencedirect.com/journal/journal-of-magnetic-resonance-open

Research article

Cumulant expansion framework for internal gradient distributions tensors

Leonardo A. Pedraza Pérez [a,b], Gonzalo A. Álvarez [a,c,d,*]

[a] Instituto Balseiro, CNEA, Universidad Nacional de Cuyo, S. C. de Bariloche, 8400, Argentina
[b] Centro Atómico Bariloche, CNEA, S. C. de Bariloche, 8400, Argentina
[c] Centro Atómico Bariloche, CONICET, CNEA, S. C. de Bariloche, 8400, Argentina
[d] Instituto de Nanociencia y Nanotecnologia, CNEA, CONICET, S. C. de Bariloche, 8400, Argentina

ARTICLE INFO

Keywords:
Internal magnetic field gradients
Diffusion-weighted imaging
Susceptibility-weighted imaging
Tissue microstructure
Porous media

ABSTRACT

Magnetic resonance imaging is a powerful, non invasive tool for medical diagnosis. The low sensitivity for detecting the nuclear spin signals, typically limits the image resolution to several tens of micrometers in preclinical systems and millimeters in clinical scanners. Other sources of information, derived from diffusion processes of intrinsic molecules such as water in the tissues, allow getting morphological information at micrometric and submicrometric scales as potential biomarkers of several pathologies. Here we consider extracting this morphological information by probing the distribution of internal magnetic field gradients induced by the heterogeneous magnetic susceptibility of the medium. We use a cumulant expansion to derive the dephasing on the spin signal induced by the molecules that explore these internal gradients while diffusing. Based on the cumulant expansion, we define internal gradient distributions tensors (IGDT) and propose modulating gradient spin echo sequences to probe them. These IGDT contain microstructural morphological information that characterize porous media and biological tissues. We evaluate the IGDT effects on the magnetization decay with typical conditions of brain tissue and show that their effects can be experimentally observed. Our results thus provide a framework for exploiting IGDT as quantitative diagnostic tools.

1. Introduction

Magnetic resonance imaging (MRI) has proven to be a powerful technique for non-invasive medical diagnosis. The implementation of MRI techniques usually limits the spatial resolution to millimeters in clinical scanners and to tens of micrometers in preclinical systems. However, the monitored nuclear spins can probe smaller spatial scales. The molecular diffusion in complex compartmentalized media is deeply affected by its microstructure. The Brownian motion of spin-bearing molecules is modulated by morphological parameters allowing the extraction of quantitative information of biological tissues and porous media [1,2]. For example tortuosity coefficients [3], axon diameters [4–9], cell size-distributions [10–13], intra/extra cellular volume fraction [14–16] can be inferred. Other methods exploit magnetic tissue properties, as the magnetic susceptibility, to generate contrasts that can unveil the tissue microstructure [17–24].

Based on these principles, diffusion-weighted images (DWI) display information about the motion of water molecules within tissues [25]. DWI has become a common diagnostic tool in clinical practice. For instance, the most established clinical indication for DWI is the assessment of cerebral ischemia [26]. DWI has been also used to monitor lesion aggressiveness and tumor response in oncology imaging [27]. Its extension to diffusion tensor imaging (DTI), based on estimating the components of the apparent diffusion coefficient (ADC) along multiple directions, enables to determine tissue microstructure anisotropies which are very useful for tracking brain connectivity [28–31] and monitor physiological white-matter changes in multiple sclerosis [32]. Nevertheless, there are cases where the anisotropy of the apparent diffusion tensor is small, as occurs in wide compartments or in fiber crossing regions in brain, and the application of DTI it is thus limited [33,34].

Alternatively, susceptibility-weighted imaging (SWI) exploits the effect of magnetic susceptibility variations in tissues, to generate high resolution (0.3 mm) anatomical images in high field scanners (> 7 T) [35]. Tissue susceptibility variations are encoded in the amplitude and phase of the magnetic resonance (MR) signal. Using this information it is possible to suppress or enhance spectral components and modify the contrast of different tissues. These concepts have been used for water/fat separation [36,37], MR angiography [38–40] and gray/white-matter contrast [41]. Its application as disease biomarker is highly encouraging based on observing image changes due to iron and calcium concentration variations, and for axon demyelination witness [42–44]. However, to attain this quantitative information it is often required the rotation of the studied subject [45].

* Corresponding author at: Centro Atómico Bariloche, CONICET, CNEA, S. C. de Bariloche, 8400, Argentina.
E-mail address: gonzalo.alvarez@conicet.gov.ar (G.A. Álvarez).

https://doi.org/10.1016/j.jmro.2023.100136
Received 3 April 2023; Received in revised form 28 September 2023; Accepted 11 October 2023
Available online 16 October 2023

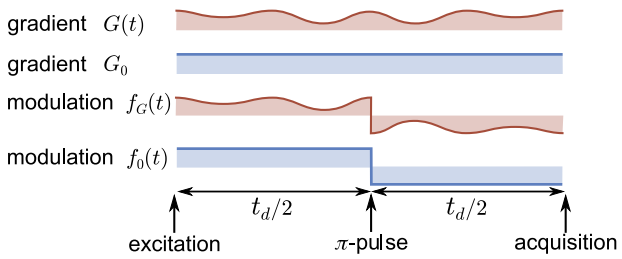

Fig. 1. Scheme for the effective applied gradient modulation function $f_G(t)$ and internal gradient modulation $f_0(t)$, based on an arbitrary applied gradient waveform $G(t)$ and a Hahn-echo sequence for modulating the internal gradient G_0. The RF π-pulse of the Hahn-echo sequence induces a sign inversion of the applied and internal gradient modulations.

Biological tissues have very complex structures and compartmentalization heterogeneities due to different molecular compositions. The intrinsic heterogeneity is imitated by the magnetic susceptibility changes along the tissue structure [46–50]. In the presence of an external magnetic field, the susceptibility discontinuities induce internal magnetic field gradients. These internal or background gradients generate measurable effects on the MR signal [51]. Since then, many authors have studied these effects on the MR signal in multiple contexts. At the beginning their were found as a source of distortions of ADC measurements, and several efforts were proposed for attaining more accurate measurement by mitigating their effects [51–53]. Then, they were found as a useful source of information as they are correlated with the microstructural features of minerals and biological tissues. For example, the effective dimensionality of the media where the particles are diffusing can be identified by the scaling laws of the ADC with the diffusion time [54]. More recently, normal and anomalous diffusion were shown to evidence differences between their MR signal decay in presence of internal gradient effects [55]. More related with the goal of this work, the correlation between internal gradients and the media microstructure allows characterizing pore size distributions [56–60] as well as microstructure morphological anisotropy [49,61,62].

These techniques are specially useful when DTI fails due to diffusion scenarios that are almost isotropic. More importantly, in contrast to quantitative SWI, the statistical characterization of internal gradient distributions can be done without reorienting the subject with respect to the direction of the main magnetic field, thus allowing to extract anisotropy information based on susceptibility heterogeneities in tissues and materials [49,61].

Brain physiology is also regulated by an assemblage of molecules and structures as the myelin sheath of axons, with significant magnetic susceptibility changes with respect to the surrounding medium. The degree of axon myelination has been shown to significantly affect the transverse relaxation time and spin phases in white matter [22,23]. Therefore, it is expected that internal gradient distributions also show correlation with the amount of myelin in such tissues [35,63–65], thus being a potential biomarker of degenerative diseases.

In this article, we provide a perturbative framework to characterize and determine internal gradient distributions by their first statistical moments. These moments define internal gradient distributions tensors (IGDT) that provide information about the media anisotropy. We formalize previous works that evidence these IGDT [49,61,65,66], based on a cumulant expansion of the spin dephasing beyond a Gaussian phase approximation. The framework presented here allows to formalize the IGDT-expansion previously reported in Ref. [49] based on a phenomenological approach. Moreover, it allows to introduce new relevant terms in the perturbative expansion, and thus gives an estimation of the errors based on the next order of the expansion. Here we consider an *internal gradient ensemble model*, where spin-bearing molecules diffuse in presence of an effective gradient. This effective gradient is determined by the average gradient seen by the spins along their diffusion trajectory [17]. The molecular diffusion is approximated as a Gaussian process allowing the simplification of high order correlations of the spin-bearing particle displacement. Then, the magnetization signal can be expressed as an expansion of IGDT of different ranks. The IGDT may have subtle effects on the magnetization signal decay, thus we exploit this IGDT-expansion to design Modulated Gradient Spin-Echo (MGSE) sequences [25,67] that use cross-correlations between an applied and the internal gradient to enhance their contributions on the MR signal decay [49]. These MGSE sequences encode the internal gradient information on the diffusion weighting decay rather than on a phase-shift of the magnetization signal, as the latter is removed in contrast to previous methods. We perform a combination of analytical and numerical analyses to predict the feasibility of determining the IGDT in realistic conditions using typical brain tissue properties. We also discuss the validity of the proposed framework.

The article is structured as follows: in Section 2 we describe the physical problem and the considered *internal gradient ensemble model*; Section 3 introduces the cumulant expansion framework for the magnetization decay and the derivation of the IGDT-expansion; in Section 4 we propose a method for measuring the IGDT and design MGSE sequences to enhance the IGDT effects on the magnetization decay; Section 5 discusses the feasibility of measuring the IGDT for conditions similar to those founds in brain tissue; in Section 6 we discuss the scope and limitations of the considered model for characterizing the internal gradients; finally, in Section 7 we summarize the results and discuss some conclusions and outlooks.

2. Spins diffusing in an inhomogeneous field

2.1. Spin phase modulated by MGSE sequences and internal gradients

We consider an heterogeneous medium in presence of a static magnetic field $\boldsymbol{B}_0$ in the z direction. Due to inhomogenities of the magnetic susceptibility in the sample, the effective magnetic field becomes also inhomogeneous leading to local field variations $\Delta\boldsymbol{B}_0(\boldsymbol{x})$ that depends on the spatial position $\boldsymbol{x}$. The typical magnetic field variations induced by the magnetic susceptibility changes in porous media are of order $\approx 10^{-6}\boldsymbol{B}_0$ [20]. As these local field variations are significantly weaker than the static magnetic field strength, we only need to consider the z component of that local field, $\Delta B_0(\boldsymbol{x})$. Since $\Delta B_0(\boldsymbol{x})$ intrinsically depends on the microstructure morphology of the medium, we are interested to probe it to extract sub-voxel morphological information. As these field variations originate internal or background gradients $\boldsymbol{G}_0(\boldsymbol{x}) = \nabla\Delta B_0(\boldsymbol{x})$, with ∇ being the differential operator with respect to $\boldsymbol{x}$, they can be probed with the nuclear spin of molecules diffusing within these internal field gradients [48].

The Brownian motion of spin-bearing particles in a constant magnetic field gradient induces spin dephasing that cannot be fully refocused by spin-echo based sequences [68–70]. This dephasing thus leads to a magnetization decay that is typically used to probe the molecular diffusion in porous media [1,25,71–73]. The temporal diffusion process can be characterized by applying magnetic field gradients that vary over time with a modulation function $f_G(t)$ [74]. Thus, the phase acquired by a diffusing spin-bearing particle during a diffusion time t_d depends on the spin-bearing particle trajectory $\boldsymbol{x}(t)$, the internal field ΔB_0 and the applied gradient $\boldsymbol{G}$ as

$$\phi\left[t_d, \boldsymbol{x}(t), \Delta B_0\right] = \gamma \int_0^{t_d} dt' \left\{\boldsymbol{x}(t')\cdot\boldsymbol{G} f_G(t') + f_0(t')\Delta B_0[\boldsymbol{x}(t')]\right\}, \tag{1}$$

where γ is the gyromagnetic ratio of the nucleus. The sign of the internal field can be controlled by radio-frequency (RF) π-pulses and it is described by the modulation function $f_0(t)$. Both modulation functions, $f_G(t)$ and $f_0(t)$, are normalized such that $\max|f(t)| = 1$. The RF π-pulses globally affect the phase evolution of the spins. Each of these pulses effectively switches also the sign of the applied gradient in the toggling frame representation of the spins [48,49]. The considered

modulation $f_G(t)$ includes the effects of the total modulation due to the applied gradient control and the effective sign switches induced by the RF π-pulses. Thus, $f_G(t)$ denotes the effective modulation of the applied gradient interaction with the spins, see Fig. 1. Here we consider MGSE sequences [25,67], where the modulating functions satisfy

$$\int_0^{t_d} dt' f(t') = 0. \tag{2}$$

2.2. Internal gradient ensemble model

An exact and rigorous treatment that describes the phase accumulation of Eq. (1) for a spin ensemble is in general very complex. We here assume that the spin phase accumulation is induced by an effective and spatially constant internal field gradient $\boldsymbol{G}_0$ that is probed by the spin bearing particle during the diffusion time t_d [17] (see Fig. 2). Then, the spin phase is simplified to the form

$$\phi\left[t_d, \boldsymbol{x}(t), \boldsymbol{G}_0\right] = \gamma \int_0^{t_d} dt' \boldsymbol{x}(t') \cdot \left\{\boldsymbol{G} f_G(t') + \boldsymbol{G}_0 f_0(t')\right\}. \tag{3}$$

When the diffusion distance is short compared with the internal gradient correlation length, it is expected that the internal gradient variations are negligible. Then, $\boldsymbol{G}_0$ is given by the local gradient at the particle position. Instead, when the diffusion distance is comparable or larger than the internal gradient correlation length, $\boldsymbol{G}_0$ is determined by an effective gradient resulting from a motional average of spin-bearing particles. This internal gradient $\boldsymbol{G}_0$ may be different for each particle depending on their position and diffusion pathway. We thus consider an ensemble of spin-bearing particles, and an ensemble of internal gradients leading to what we call the *internal gradient ensemble model* (Fig. 2). In Section 6 we discuss the scope and limitations of this model assumptions and in Appendix A we provide an analysis of its validly.

The only relaxation mechanism of the spin phase that we consider here is the diffusion process in presence of magnetic field gradients. The total spin magnetization is given by the spin ensemble average that involves all possible realization of the spin's accumulated phase. Considering the introduced *internal gradient ensemble model*, the spin ensemble average is separated in the average of all possible fluctuating diffusion paths and the average over the distribution of the internal magnetic field gradients as

$$M(t_d) = \left\langle e^{i\phi[t_d, \boldsymbol{x}(t), \boldsymbol{G}_0]} \right\rangle_{\phi} \approx \left\langle e^{i\phi[t_d, \boldsymbol{x}(t), \boldsymbol{G}_0]} \right\rangle_{x, G_0}. \tag{4}$$

Here, the brackets $\langle\cdot\rangle_{\phi}$ and $\langle\cdot\rangle_{x,G_0}$ denote the ensemble average over the spin's accumulated phase, and the double average over the particle displacement paths $\boldsymbol{x}(t)$ and the distribution of internal gradients $\boldsymbol{G}_0$ respectively. Notice that in general the equality of the average procedures in Eq. (4) does not hold, as medium heterogeneities might generate correlations between the internal gradients and the particle diffusion process. An exact analytical solution is very complex and depends on the particular correlation between the stochastic process that defines the convoluted correlation between $\boldsymbol{x}(t)$ and $\boldsymbol{G}_0(x)$. Here, in order to attain analytical solutions and focus on the effects of the internal gradients distributions, we assume a simple model that neglects the correlations between internal gradient disorder and particle diffusion (see Appendix A).

Fig. 2 shows a schematic representation of these assumptions to describe the internal gradient distributions. A realistic model for single random realizations of spin-bearing particles moving freely within a space with internal gradient distributions is shown in Fig. 2a. Along the Brownian motion paths, the spins interact with different gradient strengths depending on their instantaneous spatial position. Our simplified model, to consider the effects of the motional averaging, is shown schematically in Fig. 2b, where we assume that, during the diffusion probing time t_d, a spin diffuses within a spatial region that is represented by an effective and constant magnetic field gradient G_0. Then, the ensemble of constant gradient strengths considered in Eq. (4)

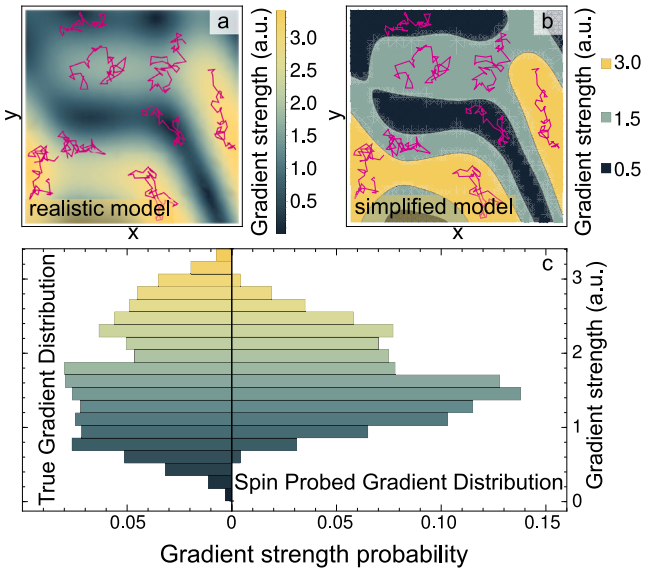

Fig. 2. Schematic representation of the *internal gradient ensemble model*. The internal gradient strengths are shown in colors represented in arbitrary units by the color bars. Realizations of the stochastic path of the Brownian motion of spin-bearing particles are shown with pink solid lines. (a) The gradient strength of a realistic model where a spin particle can diffuse freely in an inhomogeneous magnetic field. (b) Scheme for the simplified model where we assume a spin-bearing particle moves in a effective and constant gradient. (c) Comparison between the true gradient distribution associated to panel (a) and the effective gradient distribution probed by the diffusing spin-bearing particles schematized in (b). For the latter, we consider uniformly distributed spins that diffuse during a time t_d achieving a root mean square displacement $\sqrt{\left\langle (\boldsymbol{x}(t) - \langle \boldsymbol{x} \rangle)^2 \right\rangle}$ much lower than the boundary length of the simulation matrix. Notice that the effective gradient distribution and the real spatial distribution of these constant gradients are not equivalent. (For interpretation of the references to color in this figure legend, the reader is referred to the web version of this article.)

accounts for the distribution of particles in the different gradient field strengths. Fig. 2c shows how a realistic internal gradient distribution is approximated by the one determined by the *internal gradient ensemble model*. Further considerations of the regimes where this gradient ensemble distribution can be used and mimick the real distribution are discussed in Section 6.

3. Cumulant expansion framework for internal gradient distributions

3.1. Cumulant expansion for the spin dephasing

The fluctuating spin phase in presence of a constant gradient typically follows a Gaussian distribution [75,76]. However, due to the internal gradient distribution, the accumulated spin phase defined in Eq. (3) deviates from the Gaussian assumption. We thus determine the ensemble average of Eq. (4) by a cumulant expansion of the spin phase [77,78]

$$\ln M(t_d) = -\frac{1}{2}\left\langle\left\langle \phi(t_d)^2 \right\rangle\right\rangle + \frac{1}{4!}\left\langle\left\langle \phi(t_d)^4 \right\rangle\right\rangle - \frac{1}{6!}\left\langle\left\langle \phi(t_d)^6 \right\rangle\right\rangle + \cdots. \tag{5}$$

Here, the double brackets $\langle\langle \phi^n \rangle\rangle$ denote the nth order cumulant for the random variable ϕ.

Following the *internal gradient ensemble model* introduced in Section 2.2, we separate the average of the spatial position due to the diffusion process from the average over the internal gradient distribution. The second order cumulant is thus

$$\begin{aligned}\left\langle\left\langle \phi(t_d)^2 \right\rangle\right\rangle &= \left\langle \Delta\phi\left[\boldsymbol{x}(t_d), \boldsymbol{G}_0\right]^2 \right\rangle_{x, G_0} \\ &= \beta_{ij}^{GG}(t_d) G_i G_j + \beta_{ij}^{00}(t_d) \left\langle \boldsymbol{G}_0 \boldsymbol{G}_0 \right\rangle_{ij} + 2\beta_{ij}^{0G}(t_d) G_i \left\langle \boldsymbol{G}_0 \right\rangle_j,\end{aligned} \tag{6}$$

where $\Delta\phi = \phi - \langle\phi\rangle$ is the deviation from the mean accumulated spin phase. We assume that the system is at the stationary state, *i.e.* the probability density functions of the particles are invariant under time translation. Then, the average of Eq. (3) over the particle positions gives $\langle \boldsymbol{x}(t)\rangle = \text{const}$. Hence, as we are considering MGSE sequences that satisfy Eq. (2) to control the phase evolution, the mean accumulated spin phase vanishes

$$\langle\phi(t)\rangle = 0. \tag{7}$$

We use the Einstein sum convention in Eq. (6), where the indexes $i, j = x, y, z$ represent the three spatial directions. The averages $\langle \boldsymbol{G}_0\rangle_j$ and $\langle \boldsymbol{G}_0\boldsymbol{G}_0\rangle_{ij}$ denote the matrix elements of the first two moments of the internal gradient distribution. The attenuation matrices

$$\begin{aligned}\boldsymbol{\beta}^{GG}(t_d) =& \gamma^2 \int_0^{t_d} dt_1 \int_0^{t_d} dt_2 f_G(t_1) f_G(t_2) \langle \Delta\boldsymbol{x}(t_1)\Delta\boldsymbol{x}(t_2)\rangle \\ =& \gamma^2 \int_{-\infty}^{\infty} \frac{d\omega}{2\pi} \left|F_G(\omega, t_d)\right|^2 \boldsymbol{S}(\omega),\end{aligned} \tag{8}$$

$$\begin{aligned}\boldsymbol{\beta}^{00}(t_d) =& \gamma^2 \int_0^{t_d} dt_1 \int_0^{t_d} dt_2 f_0(t_1) f_0(t_2) \langle \Delta\boldsymbol{x}(t_1)\Delta\boldsymbol{x}(t_2)\rangle \\ =& \gamma^2 \int_{-\infty}^{\infty} \frac{d\omega}{2\pi} \left|F_0(\omega, t_d)\right|^2 \boldsymbol{S}(\omega)\end{aligned} \tag{9}$$

and

$$\begin{aligned}\boldsymbol{\beta}^{0G}(t_d) =& \gamma^2 \int_0^{t_d} dt_1 \int_0^{t_d} dt_2 f_0(t_1) f_G(t_2) \langle \Delta\boldsymbol{x}(t_1)\Delta\boldsymbol{x}(t_2)\rangle \\ =& \gamma^2 \int_{-\infty}^{\infty} \frac{d\omega}{2\pi} \Re\left[F_0(\omega, t_d) F_G^*(\omega, t_d)\right] \boldsymbol{S}(\omega)\end{aligned} \tag{10}$$

are overlap matrix functions that include all the temporal dependence of the magnetization decay. They are associated to the self-correlation tensor function of the spin displacement $\langle \Delta\boldsymbol{x}(t_1)\Delta\boldsymbol{x}(t_2)\rangle$ and to the gradient modulation functions $f_0(t)$ and $f_G(t)$. We consider modulation functions independent of the gradient direction. Here the instantaneous displacement $\Delta\boldsymbol{x}(t) = \boldsymbol{x}(t) - \langle\boldsymbol{x}\rangle$ is the deviation from its average value. These overlap matrix functions are also written in terms of their Fourier representations, where the Fourier transform of the gradient modulation functions is

$$F(\omega, t_d) = \int_0^{t_d} dt' \, e^{i\omega t'} f(t') \tag{11}$$

and, using the Wiener–Khinchin theorem, the displacement power spectrum matrix is

$$S_{ij}(\omega) = \int_{-\infty}^{\infty} dt' \, e^{i\omega t'} \left\langle \Delta x_i(t')\Delta x_j(0)\right\rangle, \tag{12}$$

assuming that the system is in the stationary state.

The Fourier representation based on the displacement power spectrum defines the dephasing of the spin signal from the overlap between a filter function $|F(\omega, t)|^2$ that depends on the gradient control and the frequencies modes distribution of the diffusion process $\boldsymbol{S}(\omega)$ [79,80]. Thus, the filter functions $|F(\omega, t)|^2$ can select what frequency component of the displacement power spectrum affects the dephasing.

Hence, the overlap matrix functions $\boldsymbol{\beta}(t)$ can be tailored to probe the interaction of the diffusing spin-bearing particles with the modulated gradients [48,49]. The matrices $\boldsymbol{\beta}^{GG}(t)$ and $\boldsymbol{\beta}^{00}(t)$ quantify the spin's interaction with the applied and background gradients respectively, and $\boldsymbol{\beta}^{0G}(t)$ quantifies a cross-interaction of the spins with the applied and background gradients [49].

The next non-Gaussian correction of Eq. (5) is the 4th order cumulant $\left\langle\left\langle\phi(t_d)^4\right\rangle\right\rangle$. This cumulant involves four time self-correlation tensor functions such as $\langle \Delta\boldsymbol{x}(t_1)\Delta\boldsymbol{x}(t_2)\Delta\boldsymbol{x}(t_3)\Delta\boldsymbol{x}(t_4)\rangle$, that can be simplified in terms of two times ones $\langle \Delta\boldsymbol{x}(t_1)\Delta\boldsymbol{x}(t_2)\rangle$ for Gaussian diffusion processes for the spin-bearing particle trajectory $\boldsymbol{x}(t)$.

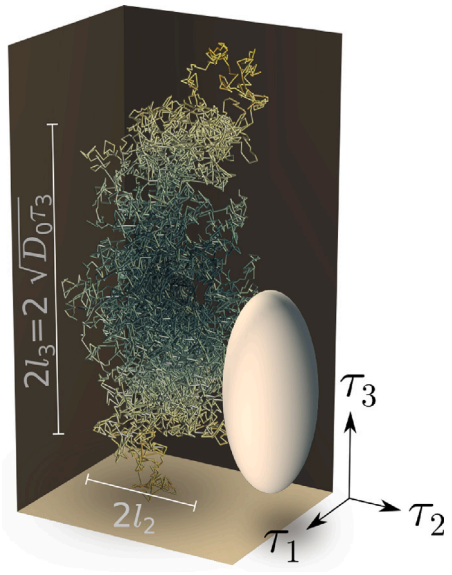

Fig. 3. Schematic representation of anisotropic diffusion due to anisotropic restriction lengths. The spin trajectory in space is restricted, described by a OU process with restriction lengths $l_3 > l_2 = l_1$, where $l_i^2 = D_0\tau_i$. The ellipsoid represents the corresponding correlation time tensor $\boldsymbol{\tau}_c$.

3.2. Diffusion translation as a 3-dimensional Ornstein-Uhlembeck process

According to the *internal gradient ensemble model*, the random variable describing the diffusion motion is independent of the gradient distribution. Thus, to obtain analytical results we model the spin-bearing particles diffusion as a Gaussian and Markovian process according to the assumptions discussed below. This diffusion model allow us to simplify the high order self-correlation tensor function that appears in Eq. (5).

As typically assumed when modeling diffusion processes in restricted compartments, we require the diffusion propagator to be stationary when diffusion time tends to infinity [81]. In one spatial dimension, the only Gaussian, Markovian and stationary process is the Ornstein–Uhlenbeck (OU) process [82,83]. In the three-dimensional space, the OU process preserves these properties, therefore we consider this model of diffusion that allows to perform analytical calculations.

In a general restricted media, the displacement correlation function along a given direction is given by

$$\langle \Delta x(0)\Delta x(t)\rangle = D_0 \sum_k b_k \tau_k e^{-|t|/\tau_k}, \tag{13}$$

where the coefficients b_k and characteristic times τ_k account for the specific geometry of the compartment [84–86]. Typically, the first of these exponential decays is the most significant, dominating the spin signal evolution [74,87,88]. The correlation function of the OU process is $\langle \Delta x(0)\Delta x(t)\rangle = D_0\tau_c e^{-|t|/\tau_c}$ with the characteristic correlation time τ_c [82]. Thus, modeling the diffusion with an OU process is equivalent to approximate the correlation function of Eq. (13) to the one given by its dominant term.

Based on this assumption, the effective restriction length l_c of the microstructure compartment in which the diffusion is taking place, can be defined as the variance of the stationary displacement distribution of the OU process. This restriction length is defined by the correlation time via the equation $l_c^2 = D_0\tau_c$ [25]. The restriction length l_c and the geometric size of the compartment depend on its shape. For the example of cylinders oriented perpendicular to the direction of the magnetic field gradient, a good approximation is $l_c = 0.37d$, where d is the cylinder diameter [74,79,86,87].

The three-dimensional version of the OU process [89] accounts for anisotropic diffusion processes that are also typically found in

$$\ln M(t_d) = -\frac{1}{2}G_i\beta_{ij}^{GG}(t_d)G_j - G_i\beta_{ij}^{0G}(t_d)\langle \boldsymbol{G}_0\rangle_j - \frac{1}{2}\beta_{ij}^{00}(t_d)\langle \boldsymbol{G}_0\boldsymbol{G}_0\rangle_{ij} + \frac{1}{2}G_iG_l\beta_{ij}^{0G}(t_d)\beta_{lk}^{0G}(t_d)\langle \Delta\boldsymbol{G}_0\Delta\boldsymbol{G}_0\rangle_{jk} + G_i\beta_{ij}^{0G}(t_d)\beta_{lk}^{00}(t_d)\langle \boldsymbol{G}_0\rangle_l\langle \Delta\boldsymbol{G}_0\Delta\boldsymbol{G}_0\rangle_{jk} + \frac{1}{2}\beta_{ij}^{00}(t_d)\beta_{kl}^{00}(t_d)\langle \boldsymbol{G}_0\rangle_i\langle \boldsymbol{G}_0\rangle_l\langle \Delta\boldsymbol{G}_0\Delta\boldsymbol{G}_0\rangle_{jk} + \frac{1}{2}G_i\beta_{ij}^{0G}(t_d)\beta_{lk}^{00}(t_d)\langle \Delta\boldsymbol{G}_0\Delta\boldsymbol{G}_0\Delta\boldsymbol{G}_0\rangle_{jkl} + \frac{1}{2}\beta_{ij}^{00}(t_d)\beta_{lk}^{00}(t_d)\langle \boldsymbol{G}_0\rangle_i\langle \Delta\boldsymbol{G}_0\Delta\boldsymbol{G}_0\Delta\boldsymbol{G}_0\rangle_{jkl} + \mathcal{O}\left[\left\langle \Delta G_0^4\right\rangle\right], \tag{16}$$

Box I.

porous media and biological tissues [28,29,31]. In order to generate a quantitative model that introduces the microstructure morphology, we first consider that the free diffusion coefficient is isotropic leading to the tensor $\boldsymbol{D}_0 = D_0\boldsymbol{I}$. The anisotropy of the diffusion process is thus only due to the compartment morphology. This anisotropy is introduced from the different correlation times along the different spatial directions in the displacement self-correlation tensor

$$\langle \Delta\boldsymbol{x}(t)\Delta\boldsymbol{x}(0)\rangle = D_0\boldsymbol{\tau}_c\exp\left(-\boldsymbol{\tau}_c^{-1}|t|\right). \tag{14}$$

Here, the correlation-time tensor $\boldsymbol{\tau}_c$ has as eigenvalues the diffusion correlation times τ_i along the principal axes of the compartment geometry (Fig. 3). The Fourier transform of the displacement self-correlation tensor gives the three-dimensional displacement power spectrum

$$\boldsymbol{S}(\omega) = 2D_0\left(\boldsymbol{\tau}_c^{-2} + \boldsymbol{I}\omega^2\right)^{-1}. \tag{15}$$

Thus, the anisotropy in the displacement power spectrum tensor reflects directly the anisotropy of the microstructure compartment morphology. In the following, we calculate the overlap matrix functions of Eqs. (8)–(10) based on this diffusion model.

3.3. The IGDT-expansion

Assuming that the diffusion process for the spin-bearing particle is driven by an OU process, we consider the cumulant expansion up to the first non-Gaussian correction, that is up to the 4th order cumulant of Eq. (5). The non-Gaussian effects increase with the internal gradient variance $\langle \Delta G_0^2\rangle$, where $\Delta\boldsymbol{G}_0 = \boldsymbol{G}_0 - \langle \boldsymbol{G}_0\rangle$. It is thus expected the expansion of Eq. (5) to work well if $\|\boldsymbol{G} + \langle \boldsymbol{G}_0\rangle\| \gg \sqrt{\langle \Delta G_0^2\rangle}$. Therefore, we rewrite Eq. (5) in terms of the moments of the internal gradient distribution. In general, the cumulant expansion (5) converges slowly and irregularly with the addition of higher order terms [73]. Then, to improve the convergence of the expansion up to the 4th order cumulant, we omit the internal gradient distribution moments of order higher than 3. Under these assumptions, the magnetization decay is (see Eq. (16) in Box I) where we used the Einstein notation again. The moments $\langle \boldsymbol{G}_0\boldsymbol{G}_0\cdots\rangle_{ij\ldots}$ and the central moments $\langle \Delta\boldsymbol{G}_0\Delta\boldsymbol{G}_0\cdots\rangle_{ij\ldots}$ denote the matrix elements of the IGDT. Notice that the average is taken over the internal gradient distribution, expressing the cumulant expansion of Eq. (5) in terms of the IGDT of different ranks.

The expansion of Eq. (16) involves several terms that depend on the applied gradient strength G and the IGDT of different ranks, combined with the overlap integrals between gradient modulation functions and the displacement self-correlations given by the matrices $\boldsymbol{\beta}^{GG}(t)$, $\boldsymbol{\beta}^{00}(t)$ and $\boldsymbol{\beta}^{0G}(t)$. Eq. (16) thus sets one of the main results of this article, defining what we call the IGDT-expansion. Table 1 summarize the notation we use in the following for all the terms of Eq. (16).

The assumption of Gaussian diffusion allows the simplification of the noise spectrum and its cross-correlation with the gradient modulation filters due to the factorization of high-order cumulants as products of the 2nd order overlap matrices $\boldsymbol{\beta}^{GG}(t)$, $\boldsymbol{\beta}^{00}(t)$ and $\boldsymbol{\beta}^{0G}(t)$ [see Eq. (16)]. Notice that within the *internal gradient ensemble model* assumptions, more complex, non-Gaussian diffusion models can be considered. However in those cases, the factorization of the overlap matrices on 2-rank matrices does not hold, and thus higher rank matrices have to be considered. For example, the factor $\beta_{ij}^{0G}(t)\beta_{kl}^{0G}(t)$ in the 4th term of the expansion (16) becomes $\beta_{ijkl}^{00GG}(t)$, where

$$\boldsymbol{\beta}^{00GG}(t_d) = \gamma^4\int_0^{t_d} dt_1\cdots f_0(t_1)f_0(t_2)f_G(t_3)f_G(t_4) \times \langle \Delta\boldsymbol{x}(t_1)\Delta\boldsymbol{x}(t_2)\Delta\boldsymbol{x}(t_3)\Delta\boldsymbol{x}(t_4)\rangle.$$

This example shows that in order to get analytical expression, a model for the 4-order diffusion correlator need to be defined. However, if the correlation between spin position and internal gradient holds negligible, the IGDT that contribute to the dephasing retain the same structure.

The leading term in Eq. (16) $\chi_{G^2} = -\frac{1}{2}G_i\beta_{ij}^{GG}(t_d)G_j$ only depends on the applied gradient modulation. The next term $\chi_{0G} = -G_i\beta_{ij}^{0G}(t_d)\langle \boldsymbol{G}_0\rangle_j$ is a *cross-term* involving the overlap integral of the displacement power spectrum with the applied and internal gradient modulation filters. The overlap matrix $\boldsymbol{\beta}^{0G}(t)$ can be positive, negative or null depending on the gradient modulation shapes and symmetries, unlike the attenuation matrices $\boldsymbol{\beta}^{GG}(t)$ and $\boldsymbol{\beta}^{00}(t)$ that are always positive defined. The magnitude of χ_{0G} depends on the angle between the applied gradient and the mean internal gradient, therefore it can be controlled by the applied gradient direction to probe the average internal gradient direction. Accordingly, its sign depends on the direction of $\boldsymbol{G}$. The next term $\chi_{0^2} = -\frac{1}{2}\beta_{ij}^{00}(t_d)\langle \boldsymbol{G}_0\boldsymbol{G}_0\rangle_{ij}$ is proportional to the mean square value of the background gradient, but it is insensitive to its spatial orientation.

The next relevant term is $\chi_{G^2\Delta^2} = \frac{1}{2}G_iG_l\beta_{ij}^{0G}(t_d)\beta_{kl}^{0G}(t_d)\langle \Delta\boldsymbol{G}_0\Delta\boldsymbol{G}_0\rangle_{jk}$. This is also a *cross-term* similarly to χ_{0G}, but it involves the variance IGDT $\langle \Delta\boldsymbol{G}_0\Delta\boldsymbol{G}_0\rangle$. This variance tensor provides information about the anisotropy of the internal gradient distribution widths along the different spatial directions, and thus depends on the media morphology and its orientation with respect to magnetic field $\boldsymbol{B}_0$ [49]. Then, the term $\chi_{0^2\Delta^2} = \frac{1}{2}\beta_{ij}^{00}(t_d)\beta_{kl}^{00}(t_d)\langle \boldsymbol{G}_0\rangle_i\langle \boldsymbol{G}_0\rangle_l\langle \Delta\boldsymbol{G}_0\Delta\boldsymbol{G}_0\rangle_{jk}$ depends only on the internal gradient and contains information about its distribution width. However, it is invariant under applied gradient modulations, thus it does not provide information about internal gradient anisotropy. The term $\chi_{0G\Delta^2} = G_i\beta_{ij}^{0G}(t_d)\beta_{kl}^{00}(t_d)\langle \boldsymbol{G}_0\rangle_l\langle \Delta\boldsymbol{G}_0\Delta\boldsymbol{G}_0\rangle_{jk}$ is a *cross-term* as $\chi_{G^2\Delta^2}$ and χ_{0G}, and in this case its magnitude can be controlled by the applied gradient. By suitable control of the symmetries of the gradient's modulations it may vanish. Moreover, the sign of $\chi_{0G\Delta^2}$ changes also like χ_{0G} when the direction of the applied gradient is inverted. The last two terms $\chi_{G\Delta^3} = \frac{1}{2}G_i\beta_{ij}^{0G}(t_d)\beta_{kl}^{00}(t_d)\langle \Delta\boldsymbol{G}_0\Delta\boldsymbol{G}_0\Delta\boldsymbol{G}_0\rangle_{jkl}$ and $\chi_{0\Delta^3} = \frac{1}{2}\beta_{ij}^{00}(t_d)\beta_{kl}^{00}(t_d)\langle \boldsymbol{G}_0\rangle_i\langle \Delta\boldsymbol{G}_0\Delta\boldsymbol{G}_0\Delta\boldsymbol{G}_0\rangle_{jkl}$, involve IGDT of the 3th order that give information about the skewness of the internal gradient distribution. Thus, they vanish for symmetric distributions.

4. Distilling and improving the IGDT-expansion effects on the spin dephasing

4.1. Observing IGDT terms

We aim at distilling the contribution of the different IGDT-expansion terms in Eq. (16) and maximizing their effects on the spin magnetization decay. We use MGSE sequences to avoid a phase shift induced by the mean macroscopic inhomogeneity in the magnetization signal according to Eqs. (2) and (7) [48]. We then identify four groups of terms in the IGDT-expansion $\ln M = \chi_{\text{app}} + \chi_{\text{bck}} + \chi_{\text{odd-cross}} + \chi_{\text{even-cross}}$ of Eq. (16) (see Table 1):

Table 1
Nomenclature for the different IGDT terms of the cumulant expansion, their definitions and physical description. The term descriptions in the last column give geometric interpretation assuming isotropic diffusion, *i.e.* overlap matrices $\boldsymbol{\beta}(t)$ proportional to the identity. The more general interpretation is based on considering the overlap matrices as metric tensors that modify the inner product of the gradient vectors. In this case the overlap matrices $\boldsymbol{\beta}^{GG}(t)$ and $\boldsymbol{\beta}^{00}(t)$ are real, symmetric and positive-definite while $\boldsymbol{\beta}^{0G}(t)$ may be null, negative or positive-definite depending on the gradient modulation symmetries. Given a non-singular symmetric matrix $\boldsymbol{\beta}$, we can define an inner product $(\cdot,\cdot)$ between two vectors $\boldsymbol{u}$ and $\boldsymbol{v}$ as $(\boldsymbol{u},\boldsymbol{v}) = \boldsymbol{u}\cdot\boldsymbol{\beta}\cdot\boldsymbol{v}$. Here $\boldsymbol{\beta}$ is the metric tensor and is a generalization of the traditional Euclidean inner product $\boldsymbol{u}\cdot\boldsymbol{v} = \boldsymbol{u}\cdot\boldsymbol{I}\cdot\boldsymbol{v}$. The definitions in the third column can be interpreted by this inner product generalization with a metric defined by the anisotropy of the diffusion process encoded by the $\boldsymbol{\beta}$ matrices.

IGDT groups	IGDT names	Definition	Description of the IGDT term
χ_{app}	χ_{G^2}	$-\frac{1}{2}G_i\beta^{GG}_{ij}(t)G_j$	Applied gradient weighting
χ_{bck}	χ_{0^2}	$-\frac{1}{2}\beta^{00}_{ij}(t)\langle \boldsymbol{G}_0\boldsymbol{G}_0\rangle_{ij}$	Trace-weighting of the internal gradient variance tensor
	$\chi_{0^2\Delta^2}$	$\frac{1}{2}\beta^{00}_{ij}(t)\beta^{00}_{kl}(t)\langle \boldsymbol{G}_0\rangle_i\langle \boldsymbol{G}_0\rangle_l\langle \boldsymbol{\Delta G}_0\boldsymbol{\Delta G}_0\rangle_{jk}$	Weighting of the internal gradient variance tensor in the mean internal gradient direction
	$\chi_{0\Delta^3}$	$\frac{1}{2}\beta^{00}_{ij}(t)\beta^{00}_{kl}(t)\langle \boldsymbol{G}_0\rangle_i\langle \boldsymbol{\Delta G}_0\boldsymbol{\Delta G}_0\boldsymbol{\Delta G}_0\rangle_{jkl}$	Weighting of the internal gradient distribution skewness
$\chi_{\text{odd-cross}}$	χ_{0G}	$-G_i\beta^{0G}_{ij}(t)\langle \boldsymbol{G}_0\rangle_j$	Weighting of the internal mean gradient projected into the applied gradient direction
	$\chi_{0G\Delta^2}$	$G_i\beta^{0G}_{ij}(t)\beta^{00}_{kl}(t)\langle \boldsymbol{G}_0\rangle_l\langle \boldsymbol{\Delta G}_0\boldsymbol{\Delta G}_0\rangle_{jk}$	Weighting of the internal gradient variance tensor projected in the applied and internal mean gradient directions
	$\chi_{G\Delta^3}$	$\frac{1}{2}G_i\beta^{0G}_{ij}(t)\beta^{00}_{kl}(t)\langle \boldsymbol{\Delta G}_0\boldsymbol{\Delta G}_0\boldsymbol{\Delta G}_0\rangle_{jkl}$	Cross-weighting of the internal gradient distribution skewness with the applied gradient
$\chi_{\text{even-cross}}$	$\chi_{G^2\Delta^2}$	$\frac{1}{2}G_iG_l\beta^{0G}_{ij}(t)\beta^{0G}_{kl}(t)\langle \boldsymbol{\Delta G}_0\boldsymbol{\Delta G}_0\rangle_{jk}$	Internal gradient variance tensor weighted in the applied gradient direction

(*i*) *the pure applied term* $\chi_{\text{app}} = \chi_{G^2}$;
(*ii*) *the pure background terms*: $\chi_{\text{bck}} = \chi_{0^2} + \chi_{0^2\Delta^2} + \chi_{0\Delta^3}$;
(*iii*) *the odd cross-terms* $\chi_{\text{odd-cross}} = \chi_{0G} + \chi_{0G\Delta^2} + \chi_{G\Delta^3}$;
(*iv*) and *the even cross-term* $\chi_{\text{even-cross}} = \chi_{G^2\Delta^2}$.

These terms can be probed selectively by suitable design of the gradient modulation sequence inspired on a previous proposal [49]. We can observe directly *the pure applied* and *background* gradient terms (*i* and *ii*) $\chi_{\text{app}} + \chi_{\text{bck}}$, by making null *the cross-terms* contribution described in (*iii*) and (*iv*). *The cross-terms* are null if the overlap matrix $\boldsymbol{\beta}^{0G}(t_d) = 0$, by generating an odd function for the product $f_0(t)f_G(t)$ with respect to the diffusion time $t_d/2$. This is done by exploiting the symmetries of applied and background gradient modulation to generate what we call the *symmetric sequence* as shown in Fig. 4a. Thus, the magnetization attenuation factor for this sequence is $\ln M_{\text{Sym}} = \chi_{\text{app}} + \chi_{\text{bck}}$. The *pure background* gradient effects (*ii*) can be selectively observed by a null applied gradient, *i.e.* we obtain $\ln M_{\text{Sym},\boldsymbol{G}=0} = \chi_{\text{bck}}$. Then, by subtracting its corresponding attenuation factor to the one obtained by the *symmetric sequence*, we can probe *the pure applied* gradient terms $\chi_{\text{app}} = \ln M_{\text{Sym}} - \ln M_{\text{Sym},\boldsymbol{G}=0}$.

We then increase the cross overlap matrix $\boldsymbol{\beta}^{0G}(t_d)$ contribution while keeping invariant $\boldsymbol{\beta}^{GG}(t_d)$ and $\boldsymbol{\beta}^{00}(t_d)$. This is done just by relatively shifting the applied and background gradient modulations functions, creating what we call an *asymmetric sequence* as shown in Fig. 4b. Thus, by subtracting the attenuation factors from the decaying signals between the *symmetric* and *asymmetric sequences*, we can selectively observe the *cross-terms* contributions $\chi_{\text{odd-cross}} + \chi_{\text{even-cross}} = \ln M_{\text{Asym}} - \ln M_{\text{Sym}}$. We then exploit the fact that the *odd cross-terms* change their sign by inverting the applied gradient direction, while *the even cross-terms* are invariant against this change. Again, by subtracting or adding the attenuation factors derived from the inverted directions of the applied gradient we can selectively probe *the odd cross-terms*

$$\chi_{\text{odd-cross}} = 1/2\ln M_{\text{Asym},+\mathbf{G}} - 1/2\ln M_{\text{Asym},-\mathbf{G}} \tag{17}$$

and *the even cross-term*

$$\chi_{\text{even-cross}} = 1/2\ln M_{\text{Asym},+\mathbf{G}} + 1/2\ln M_{\text{Asym},-\boldsymbol{G}} - \ln M_{\text{Sym}}. \tag{18}$$

Fig. 4c shows a scheme manifesting the described signal behaviors.

For a 3-dimensional IGDT inference, we must repeat this strategy on multiple non-collinear applied gradient directions in order to determine the IGDT terms. Inspired on the methods for reconstructing

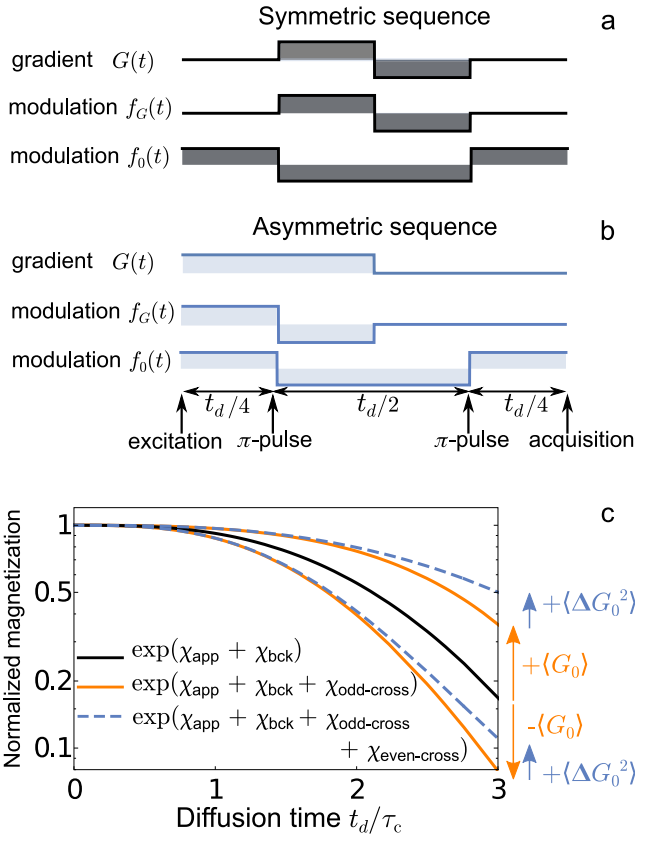

Fig. 4. Schematic representation of a *symmetric* (a), an *asymmetric sequence* (b) and the corresponding spin signals behavior based on the contribution of the different IGDT terms (c). The solid black line in (c) corresponds to the attenuation induced by the pure applied (*i*) and pure background gradients (*ii*) terms derived from the symmetric sequence. The orange solid lines add the *odd cross-terms* contributions (*iii*) to the signal attenuation. Depending on the relative direction between the applied and mean background gradient, this contribution is positive or negative. The blue dashed lines in (c) are the signal decay derived from the asymmetric sequence, that add *the even cross-term* contribution, which is proportional to the covariance tensor of the internal gradient distribution. The *even-cross terms* are always positive independent on the applied gradient direction. (For interpretation of the references to color in this figure legend, the reader is referred to the web version of this article.)

the diffusion tensor [28,29], we proposed a technique to extract $\langle \boldsymbol{G}_0 \rangle$ and $\langle \Delta\boldsymbol{G}_0 \Delta\boldsymbol{G}_0 \rangle$ in Ref. [49]. First, we need to determine the pure applied gradient overlap matrix $\boldsymbol{\beta}^{GG}(t)$ to find the correlation-time tensor $\boldsymbol{\tau}_c$ and the free diffusion coefficient D_0. The matrix $\boldsymbol{\beta}^{GG}(t)$ has six independent elements. Therefore, we must measure *the pure applied term* χ_{app} at least for six non-collinear applied gradient directions. As the attenuation terms are noisy, it is also important to increase the number of non-collinear gradient directions [33,34,90] to estimate $\boldsymbol{\beta}^{GG}(t)$ statistically using a multivariate linear regression. The correlation times in each direction and the free diffusion coefficient can be estimated by fitting the estimated $\boldsymbol{\beta}^{GG}(t)$ based on our analytic model (8).

Once these parameters are determined, we can calculate the other two overlap matrices $\boldsymbol{\beta}^{0G}(t)$ and $\boldsymbol{\beta}^{00}(t)$ in term of them using Eqs. (9), (10) and (15). With the overlap matrix $\boldsymbol{\beta}^{0G}(t)$ reconstructed, we can estimate the IGDT $\langle \Delta\boldsymbol{G}_0 \Delta\boldsymbol{G}_0 \rangle$ and the mean internal gradient vector $\langle \boldsymbol{G}_0 \rangle$ by measuring *the even cross-term* $\chi_{\text{even-cross}}$ and *the odd cross-terms* $\chi_{\text{odd-cross}}$ at several applied gradient directions and using the multivariate linear regression. While further work needs to be conducted to analyze the robustness and reliability of the IGDT estimations, we anticipate that the number of experiments required in practice would be similar to those performed for estimating the diffusion tensors and/or kurtosis tensors using multivariate linear regression.

4.2. Sequence design to enhance the IGDT contributions

The IGDT contributions may be weak. As the overlap matrix $\boldsymbol{\beta}^{0G}(t_d)$ appears as a dyadic product in *the cross-terms* $\chi_{G^2\Delta^2}$, $\chi_{0G\Delta^2}$ and $\chi_{0^2\Delta^2}$, they become more relevant than *the pure applied* and *pure background gradient* ones with increasing the diffusion time. This can be seen by considering the asymptotic behavior of the attenuation factors $\beta(t_d) \sim 2c\gamma^2 D_0 \tau_c^2 t_d$ and $\beta(t_d) \sim 2c\gamma^2 D_0 t_d^3$, for the restricted ($t_d \gg \tau_c$) and free ($t_d \ll \tau_c$) diffusion limits, respectively. Here c is a dimensionless coefficient that depends on the specific gradient modulation waveform. The first order terms that are linearly proportional to the overlap matrices $\boldsymbol{\beta}(t_d)$ are the most significant on the attenuation factor up to the following approximated time scale

$$t_{G_{tot}} = \left[c\gamma^2 D_0 \left(\boldsymbol{G} + \langle \boldsymbol{G}_0 \rangle \right)^2 \right]^{-1/3}, \tag{19}$$

for the free diffusion regime and

$$t_{G_{tot}} = \left[c\gamma^2 D_0 \left(\boldsymbol{G} + \langle \boldsymbol{G}_0 \rangle \right)^2 \tau_c^2 \right]^{-1}, \tag{20}$$

for the restricted diffusion regime. Here, $t_{G_{tot}}$ is the dephasing time associated to the magnetization decay $M(t_d) = \exp\left\{ -\frac{1}{2}\beta(t_d) \left(\boldsymbol{G} + \langle \boldsymbol{G}_0 \rangle \right)^2 \right\}$ to $1/e$, of the spin-bearing particles diffusing in a gradient $\boldsymbol{G}_{tot} = \boldsymbol{G} + \langle \boldsymbol{G}_0 \rangle$ in the respective diffusion regimes. At longer times, the higher order IGDT terms become more relevant.

The previous consideration are general for a cumulant expansion. In the following, we consider control strategies to enhance the IGDT terms contribution to the signal decay, while minimizing the loss of signal due to the pure interaction with the applied gradient. We need to enhance the terms that include the cross-overlap matrix $\boldsymbol{\beta}^{0G}(t)$ in the IGDT-expansion of Eq. (16). We thus look for conditions on the overlap matrices $\boldsymbol{\beta}^{GG}(t_d)$ and $\boldsymbol{\beta}^{0G}(t_d)$ that increase *the cross-terms* contribution with respect to *the pure applied* one.

We find that requesting the matrix difference $|\boldsymbol{\beta}^{0G}(t_d)| - \boldsymbol{\beta}^{GG}(t_d)$ to be positive-definite, enhance the IGDT terms contributions. Here, we define the modulus matrix $|\boldsymbol{\beta}|$ as the matrix whose eigenvalues are the modulus of the eigenvalues of $\boldsymbol{\beta}$. As the principal directions of all considered overlap matrices are defined by the ones of the correlation-time tensor $\boldsymbol{\tau}_c$, the positive-definite condition for $|\boldsymbol{\beta}^{0G}(t_d)| - \boldsymbol{\beta}^{GG}(t_d)$ is

$$|\beta_i^{0G}(t_d)| > \beta_i^{GG}(t_d) \quad i = 1, 2, 3, \tag{21}$$

where $\beta_i^{0G}(t_d)$ and $\beta_i^{GG}(t_d)$ are the eigenvalues of the corresponding overlap matrices. A derivation for this condition to enhance the IGDT contributions is found in Appendix B. Notice that from Eq. (16), if the vector $\boldsymbol{\beta}^{0G}(t_d)\langle \boldsymbol{G}_0 \rangle$ is orthogonal to the applied gradient, the second term vanishes independently on the relation (21). Then, the expression of Eq. (21) is a necessary but not sufficient condition.

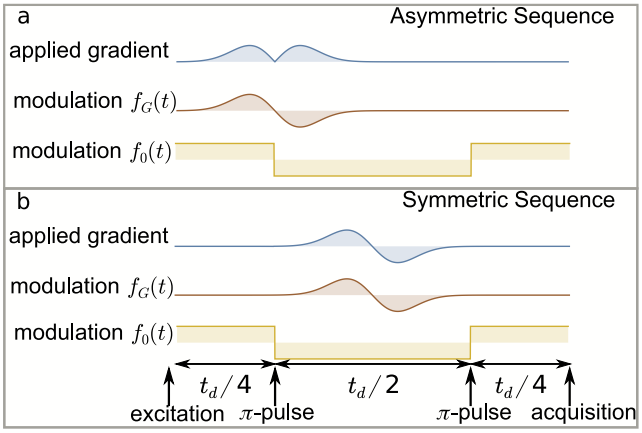

Fig. 5. Suitable design of *Symmetric* and *Asymmetric Sequences* of modulated gradients to probe the IGDTs. The sequences involve an initial excitation pulse followed by an applied gradient modulation defined by $f_G(t)$ given by Eq. (27). Together with two RF π-pulses at times $t = 1/4\,t_d$ and $t = 3/4\,t_d$ to modulate the background gradient as $f_0(t)$, determines the Gaussian derivative gradient spin-echo (GDGSE) sequence. This diffusion weighting block is then followed by an acquisition block. (a) *Asymmetric Sequence* and (b) *Symmetric Sequence*. In both sequences, the internal gradient modulation $f_0(t)$ corresponds to the one determined by the two RF pulses conforming a CPMG sequence that refocus the decoherence due to susceptibility-induced magnetic field inhomogenities. The applied gradient modulation is proportional to the first derivative of the Gaussian function as shown in Eq. (27). The spin dephasing due to interaction with the positive part of the applied gradient modulation is then refocused by the interaction with the negative part of the modulation. The modulation profile $f_G(t)$ in the *Asymmetric Sequence* is obtained by applying the gradient profile shown with the blue line in panel (b), as the RF π-pulses effectively change the sign of the phase evolution of the spins. The time interval in which the modulation $f_G(t)$ is significantly different from zero is lower than $1/2\,t_d$. (For interpretation of the references to color in this figure legend, the reader is referred to the web version of this article.)

The pure background gradient contribution is enhanced by minimizing the number of RF pulses, as its corresponding filter function lower the frequency of its dominant peak, thus maximizing the overlap with the displacement spectral density $\boldsymbol{S}(\omega)$ which is centered at zero frequency. *The cross-term* contributions are enhanced by increasing the applied gradient strength [see Eq. (16)], however this also enhance the pure applied gradient term. In order to avoid the latter effect, we increase the modulation frequency of the applied gradient to reduce the overlap of the applied gradient filter function with the spectral density, thus reducing its dephasing effects. This can be done by considering the temporal variations of $f_G(t)$ only during a small time interval with respect to the total diffusion time as shown in Fig. 5.

If the modulation frequency of the applied gradient becomes larger than the one of the background gradient modulation, the cross-filter overlap $\Re\left[F_0(\omega, TE) F_G^*(\omega, TE)\right]$ in Eq. (10) also is reduced. With the aim of increasing *the cross-terms* dephasing effect, we thus reduce the total duration of the applied gradient modulation to broaden its high-frequency peak and allow the overlap with the background gradient filter component at lower frequencies. This cross-filter overlap can be further maximized by synchronizing properly the sign changes of the applied and background gradient modulations to make a constructive interference between them as described in details in Appendix C.

In order to attain the condition of Eq. (21), we reduce the effective interaction time of the spins with the applied gradient, compared to the times they interact with the cross interference of the applied and background gradients. The effective interaction time of the background and applied gradients are the diffusion times during which the spins interact with each of these gradients,

$$T_0 = \int_0^{t_d} dt\, f_0^2(t) \tag{22}$$

and

$$T_G = \int_0^{t_d} dt\, f_G^2(t), \tag{23}$$

respectively. Similarly, the effective interaction time of *the cross-term* is the diffusion time that generates the cross interference between the applied and background gradients,

$$T_{0G} = \int_0^{t_d} dt\, f_0(t) f_G(t). \tag{24}$$

Therefore, to achieve the condition (21), we need $T_{0G} > T_G$. This latter condition can be seen more directly at the restricted diffusion limit, where we can approximate the overlap matrices as

$$\begin{aligned}\boldsymbol{\beta}^{GG}_{rest}(t_d) &\approx \boldsymbol{S}(0)\gamma^2 \int_{-\infty}^{\infty} \frac{d\omega}{2\pi} \left|F_G(\omega, t_d)\right|^2 \\ &\approx \boldsymbol{S}(0)\gamma^2 \int_0^{t_d} dt\, f_G^2(t) \\ &\approx \boldsymbol{S}(0)\gamma^2 T_G \end{aligned} \tag{25}$$

and

$$\begin{aligned}\boldsymbol{\beta}^{0G}_{rest}(t_d) &\approx \boldsymbol{S}(0)\gamma^2 \int_{-\infty}^{\infty} \frac{d\omega}{2\pi} \Re\left[F_0(\omega, t_d) F_G^*(\omega, t_d)\right] \\ &\approx \boldsymbol{S}(0)\gamma^2 \int_0^{t_d} dt\, f_0(t) f_G(t) \\ &\approx \boldsymbol{S}(0)\gamma^2 T_{0G}, \end{aligned} \tag{26}$$

being both proportional to the corresponding effective interaction times, as the displacement spectral density can be factored out from the overlap integral. A general demonstration is found in Appendix B.

Applied gradients can be arbitrary modulated in general. However, the background gradient is only modulated by applying the RF π-pulses that invert the spin phase evolution, which is encoded in the modulation function $f_0(t)$ that switches between $+1$ and -1 at every time a π-pulses is applied. To enhance *the cross-term* effect with respect to *the pure applied term,* we thus propose the implementation of smooth modulations for the applied gradient that satisfy the condition $|f_G(t)|^2 < |f_G(t)|$, and a synchronization of the sign changes of $f_0(t)$ and $f_G(t)$ such that $f_0(t) f_G(t) = |f_G(t)|$ (Fig. 5).

To get a MGSE sequence, the applied gradient modulation $f_G(t)$ must cross zero at least once. The condition $f_0(t) f_G(t) = |f_G(t)|$ can be attained by setting a smooth MGSE with an applied gradient modulation with a single refocusing echo, whose zero crossing time matches the instant of time where the RF π-pulse is applied to modulate the background gradient function $f_0(t)$. To avoid further sign inversions in $f_0(t) f_G(t)$, the applied gradient modulation $f_G(t)$ must vanish every time that a π-pulse is applied. Fig. 5a shows an example of such a modulation. Thus, all of these conditions define a general *asymmetric sequence* that enhance the IGDT *cross-term* contributions.

To probe directly the IGDT terms proportional to $\boldsymbol{\beta}^{GG}(t_d)$ and $\boldsymbol{\beta}^{00}(t_d)$, we must cancel *the cross-term* dephasing effect in Eq. (16), while keeping invariant *the pure terms*. We thus make $\boldsymbol{\beta}^{0G}(t_d) = 0$ by setting $f_G(t)$ an odd function with respect to its middle time and $f_0(t)$ an even function, again with respect to its middle time. Then, the cross-filter vanishes by matching the modulation centers of $f_G(t)$ and $f_0(t)$. Fig. 5b shows an example of such modulation sequence. The pure overlap matrices $\boldsymbol{\beta}^{GG}(t_d)$ and $\boldsymbol{\beta}^{00}(t_d)$ thus remain invariant, because temporal shifts of the corresponding modulation functions does not alter the squared modulus of their Fourier transform. This shifted modulation define a general *symmetric sequence.*

Finally, to maximize the background gradient dephasing effects with the overlap integrals $\boldsymbol{\beta}^{00}(t_d)$ and $\left|\boldsymbol{\beta}^{0G}(t_d)\right|$, we have to modulate the background gradient with a low frequency to maximize their overlap with the displacement spectral density $\boldsymbol{S}(\omega)$. We thus need a modulation sequence with the minimal possible number of pulses. As we require $f_0(t)$ to be an even function, we choose a Carr–Purcell–Meiboom–Gill (CPMG) sequence [69,70] with two pulses for its modulation. The RF π-pulses are thus applied at $t = 1/4\, t_d$ and $t = 3/4\, t_d$ respectively (Fig. 5).

In Appendix B, we show that the relation of Eq. (21) is fulfilled assuming the sequence conditions derived in this section for an arbitrary diffusion regime.

In summary, to enhance *the cross-term* effects, the background gradient modulation $f_0(t)$ has to be an even function with respect to $t_d/2$ with a minimal number of pulses. The applied gradient modulation has to be an MGSE sequence with a smooth modulation function such that $|f_G(t)| \leq 1$, with a single refocusing echo matching the zero crossing time with a π-pulse that modulate $f_0(t)$. The modulation function $f_G(t)$ has to be an odd function with respect to its middle time, *i.e.* the zero crossing time, and should vanish also at every π-pulse that modulate $f_0(t)$.

4.3. Paradigmatic example: Gaussian derivative modulation

To follow the above sequence design, we propose here a paradigmatic MGSE sequence with applied gradient modulations derived from a Gaussian function derivative. We call it the Gaussian derivative gradient spin-echo (GDGSE) modulation that allow us to obtain analytical calculations. The GDGSE sequence consists on a modulation function $f_G(t)$ determined by the first derivative of a Gaussian function centered at $t_d/2$ with a standard deviation given by a fraction $\alpha\, t_d$ of the total diffusion time t_d (see Fig. 5b)

$$f_G(t) = \frac{\sqrt{e}}{\alpha t_d}(t - t_d/2) e^{-\frac{(t-t_d/2)^2}{2\alpha^2 t_d^2}}. \tag{27}$$

Here, $\alpha \ll 1$ is a coefficient that controls the Gaussian modulation width.

The modulation function is normalized such that it satisfies $\max[f_G(t)] = 1$, so as the maximum gradient strength G is achieved. While the GDGSE allows us to obtain analytical expressions for the dephasing, its modulation is not finite along the time domain. As the applied gradient modulation decays exponentially for times $t \gg \alpha t_d$, we set the parameter $\alpha \ll 1$ to make negligible its modulation amplitude at every RF π-pulse and outside the considered diffusion time interval t_d. We thus consider negligible the modulation amplitude at the RF pulses $f_G(1/4\, t_d) = f_G(3/4\, t_d) \approx 0$ and outside the diffusion probing time. For example, by setting $\alpha = 1/15$, the modulation amplitude at the RF pulses and outside the probing time is $\lesssim 10^{-3}$. This requirement for α also provides a large frequency for the applied gradient modulation as required in Section 4.2 and, at the same time, reduces the effective interaction time of the applied gradient of Eq. (23).

The *asymmetric sequence* is obtained by shifting the modulation function $f_G(t)$ by $t_d/4$ to the left, as seen in Fig. 5a. To ensure a significant integral overlap between the applied and background gradient filters $\Re\left[F_0(\omega, t_d) F_G^*(\omega, t_d)\right]$, the coefficient α must not be too small. We found that $1/30 \lesssim \alpha \lesssim 1/10$ works well enough. To find a proper α, we need to compare the GDGSE filter maximum $|F_G(1/(\alpha t_d), t_d)|^2$ [see Eq. (D.3) in Appendix D] with the GDGSE filter value at the modulation frequency of the background gradient $2\pi/t_d$. For $\alpha = 1/15$, for example, $|F_G(2\pi/t_d, t_d)|^2 / |F_G(1/(\alpha t_d), t_d)|^2 = 0.4$.

4.4. Overlap matrix weightings for diffusion asymptotic limits

Here we consider two physically relevant asymptotic regimes to evaluate the overlap matrix weighting on the IGDT-expansion terms, the free diffusion ($t_d/\tau_c \ll 1$) and the restricted diffusion ($t_d/\tau_c \gg 1$) limits. The general expressions for the overlap integrals of Eqs. (8)–(10), can be found in Appendix D. As expected at the free diffusion regime, the behavior of the three overlap functions is cubic as a function of the diffusion time. If the condition $t_d/\tau_c \ll 1$ is fulfilled in all spatial directions, the diffusion can be assumed isotropic. The

overlap matrix weighting are thus proportional to the identity as all principal directions are equivalent. The integral overlaps becomes

$$\beta^{GG}_{free}(t_d) = 2e\sqrt{\pi}\gamma^2 D_0 \alpha^3 t_d^3 \tag{28}$$

and

$$\beta^{00}_{free}(t_d) = \frac{\gamma^2 D_0}{24} t_d^3. \tag{29}$$

As we consider $\alpha \ll 1$ to make $f_G(t+t_d/4) \approx 0$ at the edge of the interval $[0, t_d/2]$, the free diffusion limit of the cross overlap function gives the cross overlap

$$\beta^{0G}_{free}(t_d) = \sqrt{\frac{\pi e}{2}}\left(1/\alpha - 4\sqrt{\frac{2}{\pi}}\right)\gamma^2 D_0 \alpha^3 t_d^3. \tag{30}$$

Instead, at the restricted diffusion limit, all the overlap matrices are proportional to the diffusion time besides a constant matrix, *i.e.* they are lineal as a function of the diffusion time

$$\boldsymbol{\beta}^{GG}_{rest}(t_d) = e\sqrt{\pi}\gamma^2 D_0 \boldsymbol{\tau}_c^2 \alpha t_d, \tag{31}$$

$$\boldsymbol{\beta}^{00}_{rest}(t_d) = 2\gamma^2 D_0 \boldsymbol{\tau}_c^2 (t_d - 5\boldsymbol{\tau}_c). \tag{32}$$

Again, as $\alpha \ll 1$, the restricted diffusion limit of the cross overlap matrix can be approximated as

$$\boldsymbol{\beta}^{0G}_{rest}(t_d) = 4\sqrt{e}\gamma^2 D_0 \boldsymbol{\tau}_c^2 \alpha t_d. \tag{33}$$

The advantage of using the smooth gradient modulations to obtain the positive-definite condition for the matrix $|\boldsymbol{\beta}^{0G}(t_d)| - \boldsymbol{\beta}^{GG}(t_d)$ compared with sharp ones that switch the gradient sign between $\{-1, +1\}$, can be seen in these asymptotic behaviors. The ratios between the overlap matrices for $\alpha \ll 1$ are $\boldsymbol{\beta}^{0G}_{free}(t_d)/\boldsymbol{\beta}^{GG}_{free}(t_d) = \sqrt{\frac{e}{2}}\left(1/\alpha - 4\sqrt{\frac{2}{\pi}}\right)/(2e)$ ≈ 2.5 in the free diffusion limit and $\boldsymbol{\beta}^{0G}_{rest}(t_d)/\boldsymbol{\beta}^{GG}_{rest}(t_d) = 4\sqrt{e}/(e\sqrt{\pi}) \approx 1.4$ in the restricted one. On the other hand, a sharp modulation that only switches the gradient sign between $\{-1, +1\}$, can attain, at the most, the same effective interaction times for the spin interaction with the applied gradient and with the cross-interference between the applied and background gradients. Then, it is not possible to minimize the interaction effects with the applied gradient without also reducing the cross-interaction effects in the same ratio, and thus no enhancement of the cross IGDT terms is obtained.

5. The IGDT-expansion in typical brain tissue conditions

In this section we evaluate the IGDT-expansion assuming typical values of the free diffusion coefficient and correlation times seen in brain tissues. The diffusion coefficient typically belongs to the range starting from $0.8\,\mu m^2/ms$ to $2.2\,\mu m^2/ms$ for human brain [91–93] and $3\,\mu m^2/ms$ for free water at 37 °C [94]. Brain tissue microstructure sizes range for example for the axon radius, typically between the interval $0.3\,\mu m$–$3\,\mu m$ in human brain [95–97]. Assuming cylindrical geometries with a restriction radius within this range, the expected diffusion correlation time τ_c ranges from 10^{-2} ms to 10 ms, based on the Fick-Einstein relation $l_c^2 = D_0 \tau_c$.

The internal magnetic field variations are of the order $10^{-6} B_0$ [61,63,64]. Intra and extra-axonal internal gradients in white matter have shown to be mono-disperse with a distribution centered at zero with a width that is maximized in the direction perpendicular to the axon-bundle direction [49,61,63,64]. This was also demonstrated with capillary tube phantoms mimicking the axon morphology giving a internal gradient distribution-width of the order of 1 mT/m on a 1 T magnet [61]. Numerical calculations of internal gradients in axon bundles using the AxonPacking open-source software [98] and a Finite Perturber Method (FPM) [61,99], predict internal gradient distribution-widths on the range of 20–200 mT/m in a 9.4 T magnet [65]. As internal gradients scale with the tissue compartmentalization characteristic length l_c, internal gradient variations can be estimated by $\Delta G_0 \approx 10^{-6} B_0/l_c$. Then, $\Delta G_0 \approx 1000$ mT/m can be expected in brain tissues, consistently with observations in numerical simulations [65]. However, the highest internal gradient strengths are typically concentrated in small spatial regions, so that the molecular movement averages them, reducing their values effectively, thus making the standard deviation of internal gradient distribution smaller.

To evaluate the main features of the IGDT-expansion, we focus on a 1-dimensional analysis associated with the diffusion process in one of the principal axis of the correlation time tensor $\boldsymbol{\tau}_c$. The analysis is equivalent for the three principal axes, in which the only relevant aspect is how it scales with the corresponding τ_c. The signal evaluation would correspond to the one expected to be obtained in a single voxel in a MRI. According to Eq. (16), the IGDT-expansion then reduces to

$$\begin{aligned}\ln M(t_d) = &-\frac{1}{2}G^2\beta_{GG}(t_d) - G\beta_{0G}(t_d)\langle G_0\rangle - \frac{1}{2}\beta_{00}(t_d)\left\langle G_0^2\right\rangle \\ &+ \frac{1}{2}G^2\beta_{0G}^2(t_d)\left\langle \Delta G_0^2\right\rangle + G\beta_{0G}(t_d)\beta_{00}(t_d)\langle G_0\rangle\left\langle \Delta G_0^2\right\rangle \\ &+ \frac{1}{2}\beta_{00}^2(t_d)\langle G_0\rangle^2\left\langle \Delta G_0^2\right\rangle + \mathcal{O}\left[\left\langle \Delta G_0^3\right\rangle\right].\end{aligned} \tag{34}$$

To model the diffusion process, we consider an OU process in one spatial dimension and the gradient ensemble description of Section 2.2. The IGDT-expansion better approximates the real signal if the applied gradient is stronger than the standard deviation of internal gradient distribution $G \gg \Delta G_0$. Here we assume a Gaussian distribution for the internal gradients with mean $\langle G_0\rangle = 0.1G$ and standard deviation $\Delta G_0 = 0.15G$. Based on the reported values of internal magnetic field variations in brain tissue [64], we consider for our simulations two cases for the relation between the applied and internal gradients $G = 600$ mT/m, $\langle G_0\rangle = 60$ mT/m and $G = 400$ mT/m, and $\langle G_0\rangle = 40$ mT/m. The internal gradient distribution widths are thus, $\Delta G_0 = 90$ mT/m and $\Delta G_0 = 60$ mT/m respectively.

Based on Eq. (4), we first calculate the magnetization average of the spin-bearing particles diffusing in presence of a given internal gradient strength G_0. The thermal diffusion follows the OU Gaussian process as described in Section 3.2 for the spin's random phase. Then, the resulting magnetization average only depends on the second cumulant of the spin phase

$$M(t_d, G_0) = e^{-\frac{1}{2}\left\langle\left\langle \phi(t_d, G_0)^2\right\rangle\right\rangle}, \tag{35}$$

with $\left\langle\left\langle \phi(t_d, G_0)^2\right\rangle\right\rangle = G^2\beta_{GG}(t_d) + 2G_0 G\beta_{0G}(t_d) + G_0^2\beta_{00}(t_d)$. Notice that this second cumulant is equal to the one in Eq. (6) for a given G_0 value, *i.e.* without yet considering the internal gradient distribution. The overlap functions $\beta_{GG}(t_d)$, $\beta_{00}(t_d)$ and $\beta_{0G}(t_d)$ are given by the eigenvalues corresponding to the considered principal axis of the attenuation matrices of Eqs. (8)–(10). Then, we calculate the total magnetization decay by averaging Eq. (35) over the internal gradient distribution.

The magnetization signal for the *asymmetric sequence* described in Fig. 5a includes the *cross-term* in the gradient average

$$M_{\text{Asym}}(t_d) = e^{-\frac{1}{2}G^2\beta_{GG}(t_d)}\left\langle e^{-G_0 G\beta_{0G}(t_d)} e^{-\frac{1}{2}G_0^2\beta_{00}(t_d)}\right\rangle. \tag{36}$$

Instead, the cross overlap integral $\beta_{0G}(t_d)$ vanishes for the *symmetric sequence* described in Fig. 5b, and thus the magnetization signal is

$$M_{\text{Sym}}(t_d) = e^{-\frac{1}{2}G^2\beta_{GG}(t_d)}\left\langle e^{-\frac{1}{2}G_0^2\beta_{00}(t_d)}\right\rangle. \tag{37}$$

Typical relaxation times T_2 of white and gray matter in brain tissue are on the order of ~50–130 ms [100–102]. We thus evaluate the effects of the different groups of terms in the IGDT-expansion before this time scale to predict the reliability of measure them. Fig. 6 shows two relevant experimental situations, the restricted (Fig. 6a,b) and the free diffusion (Fig. 6c,d) regimes. To analyze the free diffusion regimen, we evaluate the magnetization at diffusion times shorter and comparable with the correlation time (up to $10\tau_c$). Instead, to study the restricted diffusion regimen, the MR signal is calculated up to longer times $40\tau_c$. For illustration, we assumed the free diffusion coefficient $D_0 = 2.2\,\mu m^2/ms$ in Fig. 6. The free diffusion coefficient in brain tissue

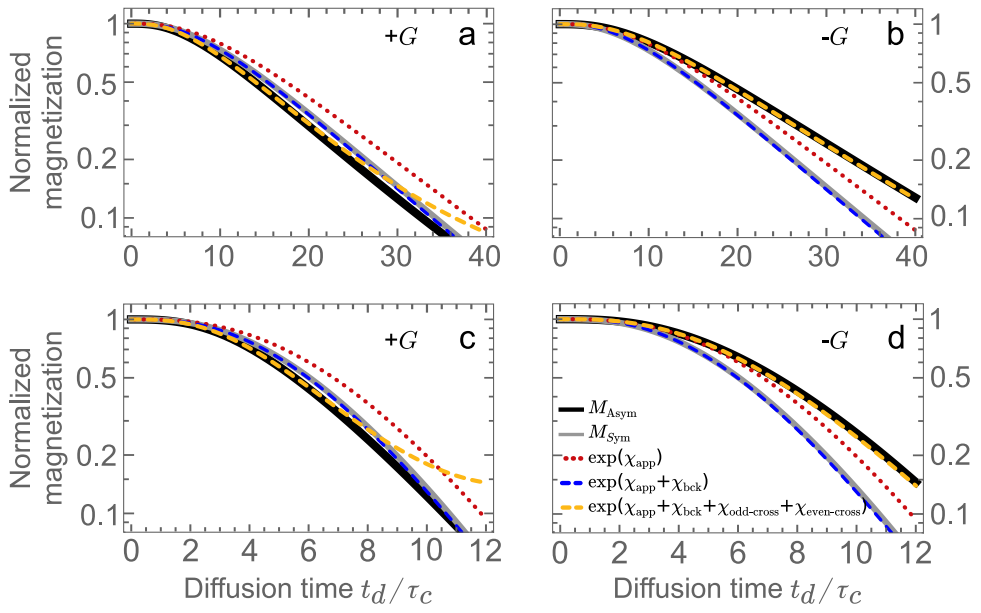

Fig. 6. Contribution of different terms of the IGDT-expansion. The solid black lines correspond to the magnetization signal produced by the *asymmetric sequence*, while the gray ones corresponds to the signal produced by the *symmetric sequence*. These signals are calculated numerically by averaging the magnetization signal with a Gaussian distribution for the background gradient G_0 with a standard deviation $\Delta G_0 = 0.15|G|$, and mean value $\langle G_0 \rangle = 0.1|G|$ in panels (a, c) and with opposite sign in panels (b, d). The red dotted line corresponds to *the pure applied gradient* contribution ($\chi_{app} = \chi_{G^2}$), the blue dashed line includes also *the pure background gradient* contribution ($\chi_{bck} = \chi_{0^2} + \chi_{0^2\Delta^2}$). The yellow dashed lines includes *the cross-terms* contributions $\chi_{odd-cross} = \chi_{0G} + \chi_{0G\Delta^2}$ and $\chi_{even-cross} = \chi_{G^2\Delta^2}$. We consider the free diffusion coefficient $D_0 = 2.2\,\mu m^2/ms$, a correlation time $\tau_c = 2\,ms$ in panels (a, b) and $\tau_c = 5\,ms$ in panels (c, d) corresponding to restriction lengths of 2 μm and 3.3 μm, and a gyromagnetic factor of $\gamma = 267\,mT^{-1}$ m s^{-1}. In panel (a) and (b) the applied gradient is $G = 600\,mT/m$ and in panels (c) and (d) $G = 400\,mT/m$. (For interpretation of the references to color in this figure legend, the reader is referred to the web version of this article.)

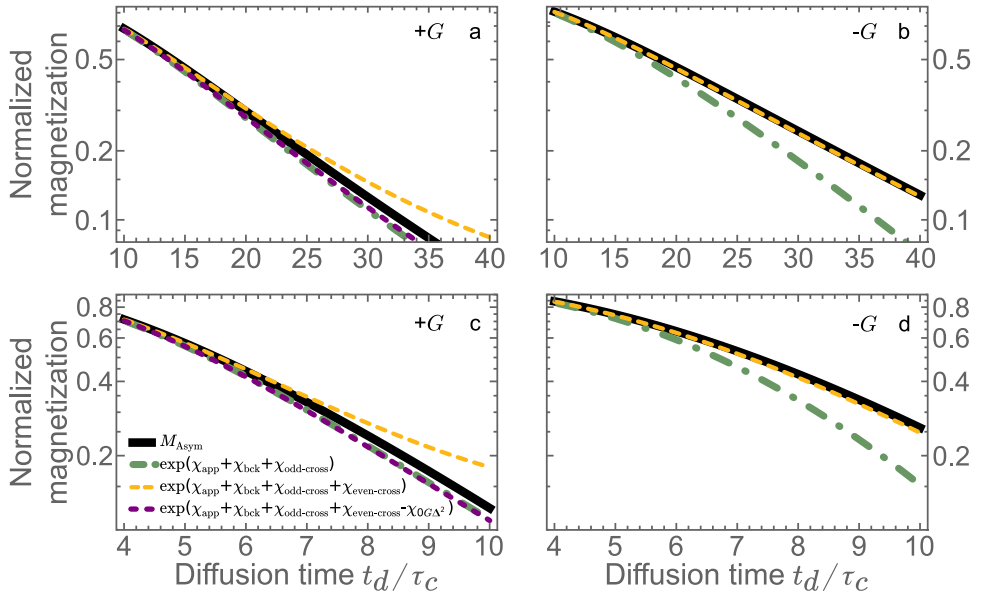

Fig. 7. Contribution of different terms of the IGDT-expansion to the magnetization signal produced by the *asymmetric sequence* (solid black lines). The green dot-dashed lines include *the pure applied* ($\chi_{app} = \chi_{G^2}$), *pure background* ($\chi_{bck} = \chi_{0^2} + \chi_{0^2\Delta^2}$) and *odd cross-terms* contribution ($\chi_{odd-cross} = \chi_{0G} + \chi_{0G\Delta^2}$). The yellow dashed lines includes also *the even cross-term* contribution $\chi_{even-cross} = \chi_{G^2\Delta^2}$. The purple dashed line consider all the terms in the yellow curve subtracting *the odd-cross term* $\chi_{0G\Delta^2} = G\beta_{0G}(t_d)\beta_{00}(t_d)\langle G_0 \rangle \langle \Delta G_0^2 \rangle$. As in Fig. 6, we consider the free diffusion coefficient $D_0 = 2.2\,\mu m^2/ms$, a correlation time $\tau_c = 2\,ms$ in panels (a, b) and $\tau_c = 5\,ms$ in panels (c, d), and a gyromagnetic factor $\gamma = 267\,mT^{-1}ms^{-1}$. In panel (a) and (b) the applied gradient is $G = 600\,mT/m$ and in panels (c) and (d) $G = 400\,mT/m$. (For interpretation of the references to color in this figure legend, the reader is referred to the web version of this article.)

is still unknown, as typically only the ADC is measured. If the free diffusion coefficient is lower than the assumed one, the magnetization decay becomes slower and thus more diffusion time is required for probing the IGDT effects. For example, if the free diffusion coefficient reduces to $D_0 \approx 0.7\,\mu m^2/ms$, the behavior of the curves of Fig. 6 would decay to 10% of the initial magnetization at 100 ms instead of 40 ms in the cases of panels a and b; and at 20 ms instead of 12 ms in the cases of panels c and d. Diffusion times that allow probing the IGDT effects are thus still accessible for the typical T_2 values of white and gray matter in brain even in this scenario.

We consider applied gradient modulations with opposite gradient directions to show the behavior of the *odd* and *even cross-terms* in the cumulant expansion. In both regimes, the magnetization of the *symmetric sequence* is well described by *the pure applied* $\chi_{app} = -\frac{1}{2}G_i\beta_{ij}^{GG}(t_d)G_j$

and *pure background gradient terms* $\chi_{\text{bck}} = \chi_{0^2} + \chi_{0^2\Delta^2} + \chi_{0\Delta^3}$ of the IGDT-expansion of Eq. (34) (see Table 1). Notice that the *pure background gradient terms* increase the magnetization decay with respect to the decay produced by only considering a *pure applied gradient term*. This is a consequence of the fact that the *background gradient term* is negative as its dominant term $\chi_{0^2} = -\frac{1}{2}\beta_{00}(t_d)\left\langle G_0^2\right\rangle$ is larger than the next term $\chi_{0^2\Delta^2} = \frac{1}{2}\beta_{00}^2(t_d)\langle G_0\rangle^2\left\langle \Delta G_0^2\right\rangle$ with opposite sign. As we discussed in Section 3.3, the lower order terms in the cumulant expansion with lower power law exponents of overlap matrices are dominant at short times $t_d < t_{G_{tot}}$, where $t_{G_{tot}}$ is given by Eqs. (19) and (20), depending on the diffusion regime. At longer times $t_d > t_{G_{tot}}$, the higher order terms become relevant and they might reduce the overall decay. By reducing the effective interaction time of the applied gradient with respect to the one of the background gradient, as done in the sequence of Fig. 5, also makes the *pure background gradient terms* more significant with respect to the pure applied terms.

Then, by including *the cross-terms* $\chi_{odd-cross} + \chi_{even-cross} = \chi_{0G} + \chi_{0G\Delta^2} + \chi_{G^2\Delta^2}$ of the expansion (34) (see Table 1), we reproduce the magnetization decay generated by the *asymmetric sequence* (Fig. 6b,d). In Fig. 6b,d there is a better convergence than in Fig. 6a,c, where the convergence is poor for $t_d > 25\tau_c$ and $t_d > 7\tau_c$, respectively. The different performance of the cumulant expansion is due to the relative direction between the applied and average background gradient that change the sign of *the odd cross-terms*.

We now analyze this effect on the signal decay. The first two *odd cross-terms* $\chi_{0G} = -G\beta_{0G}(t_d)\langle G_0\rangle$ and $\chi_{0G\Delta^2} = G\beta_{0G}(t_d)\beta_{00}(t_d)\langle G_0\rangle\left\langle \Delta G_0^2\right\rangle$ that we consider here, have opposite signs. Then, the behavior of their overall decay contribution at short times is the opposite of the one at longer times. *The even cross-term* $\chi_{G^2\Delta^2} = \frac{1}{2}G^2\beta_{0G}^2(t_d)\left\langle \Delta G_0^2\right\rangle$ is always positive and it thus always reduce the magnetization decay. As it contains a quadratic order on the attenuation overlap function, $\beta_{0G}^2(t_d)$ becomes relevant at long times $t_d > t_{G_{tot}}$ (see Eqs. (19) and (20)). This is seen at times longer than $\sim 15\tau_c$ in Fig. 7b, and at times longer than $\sim 6\tau$ in Fig. 7d, when the green dash-dotted curve starts to deviate from the exact decay (black line), and the dashed yellow line continues reproducing the expected behavior.

In Fig. 6a and c, the applied gradient has the same sign as the background gradient $\langle G_0\rangle$. *The pure background gradient term* χ_{0^2} and *the odd cross-term* χ_{0G} thus contribute by increasing the magnetization decay at short times, as both terms are negative. At longer times the behavior changes, as *the odd cross-term* $\chi_{0G\Delta^2}$ and *the even cross-term* $\chi_{G^2\Delta^2}$ now tend to reduce the magnetization decay because they are positive. In these cases, the dashed yellow line diverges from the expected signal behavior at times longer than $25\tau_c$ in Fig. 7a and at times longer than $7\tau_c$ in Fig. 7c. At these times, the terms $\chi_{0G\Delta^2}$ and $\chi_{G^2\Delta^2}$ become more relevant. This shows the slow convergence of the IGDT-expansion when the applied gradient is in the same direction of the mean background gradient. In this case, we obtain a better approximation by including only *the even cross-term* $\chi_{G^2\Delta^2}$ such as

$$\ln M(t_d) = \chi_{\text{app}} + \chi_{\text{bck}} + \chi_{0G} + \chi_{G^2\Delta^2},$$

and excluding the *odd cross-term* $\chi_{0G\Delta^2}$ or *vice versa*

$$\ln M(t_d) = \chi_{\text{app}} + \chi_{\text{bck}} + \chi_{0G} + \chi_{0G\Delta^2}.$$

Fig. 7a and c show that these expansion's approximations (purple dashed line and green dot-dashed respectively) reproduce better the predicted curve (black line).

In Fig. 6b and d, the applied gradient has the opposite sign of the average background gradient $\langle G_0\rangle$. In this case, the signal decay is reduced at short times since the leading *odd cross-term* χ_{0G} reduces the magnetization decay. At long times $t_d > t_{G_{tot}}$ (see Eqs. (19) and (20)), *the even cross-term* $\chi_{G^2\Delta^2}$ and the *odd cross-term* $\chi_{0G\Delta^2}$ have opposite behavior allowing a better convergence (Fig. 7b and d). As a result, the contrast ratio $M_{\text{Asym}}(t_d)/M_{\text{Sym}}(t_d)$ between the magnetization of the *asymmetric* and *symmetric sequences* is maximized when applied and

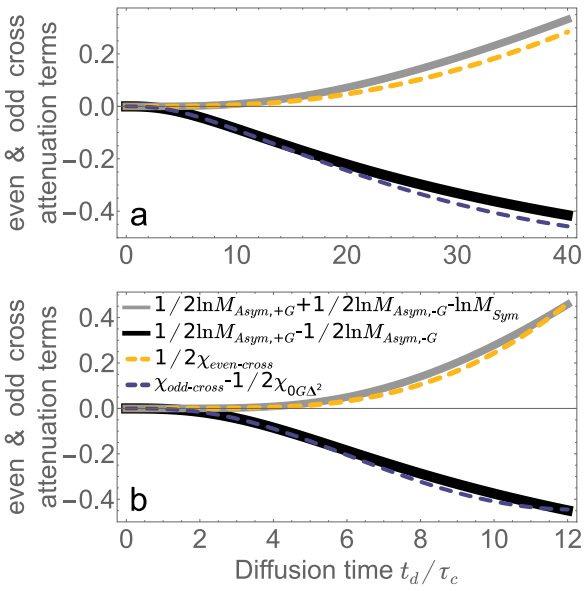

Fig. 8. Approximated *even* and *odd cross-term* attenuations when the applied gradient has the same direction as the background gradient. The gray and black solid lines gives the approximated *even* and *the odd cross-terms* following Eqs. (38) and (39) respectively, calculated from the mathematical operations between the magnetization signal of the *symmetric* and *asymmetric sequences* with the two applied gradient directions. These magnetization signals are calculated numerically by averaging the magnetization signal with a Gaussian distribution for the background gradient G_0 with a standard deviation $\Delta G_0 = 0.15|G|$, and mean value $\langle G_0\rangle = 0.1|G|$. The yellow and purple dashed lines show the corresponding *even cross-term* $1/2\chi_{\text{even-cross}} = 1/2\chi_{G^2\Delta^2}$ and *the odd cross-term* $\chi_{0G} + 1/2\chi_{0G\Delta^2} = \chi_{\text{odd-cross}} - 1/2\chi_{0G\Delta^2}$ of the left-hand-side of Eqs. (38) and (39) respectively, derived from the expansion of Eq. (34). As in Fig. 6, we consider the free diffusion coefficient $D_0 = 2.2\,\mu\text{m}^2/\text{ms}$, a correlation time $\tau_c = 2\,\text{ms}$ in panel (a) and $\tau_c = 5\,\text{ms}$ in panel (b), and a gyromagnetic factor $\gamma = 267\,\text{m T}^{-1}\,\text{m s}^{-1}$. In panel (a) the applied gradient is $G = 600\,\text{mT/m}$ and in panel (b) $G = 400\,\text{mT/m}$. (For interpretation of the references to color in this figure legend, the reader is referred to the web version of this article.)

mean background gradient are in the opposite direction compared with the case when they are in the same direction. According to the results shown in Fig. 6 we estimate a requirement for a signal-to-noise ratio within the range 10–20 at least, to measure the contribution of the four groups of terms defined in Table 1.

As shown in Fig. 7a and c, when the applied gradient has the same direction as the average background gradient, the green and purple curves are good approximation and indistinguishable between them. The green curve excludes *the even cross-term* $\chi_{G^2\Delta^2}$ and the purple one, *the odd cross-term* $\chi_{0G\Delta^2}$ from the expansion. As it is arbitrary which of these terms are excluded, we propose under this observation to approximate *the even cross-term* from the expression

$$1/2\chi_{\text{even-cross}} \approx 1/2\ln M_{\text{Asym},+\boldsymbol{G}} + 1/2\ln M_{\text{Asym},-\boldsymbol{G}} - \ln M_{\text{Sym}}, \tag{38}$$

rather than from Eq. (18) by excluding the term $\chi_{\text{even-cross}}$ from $\ln M_{\text{Asym},+\boldsymbol{G}}$. To determine *the odd cross-term*, then use the approximation

$$\begin{aligned}\chi_{0G} + 1/2\chi_{0G\Delta^2} &= \chi_{\text{odd-cross}} - 1/2\chi_{0G\Delta^2}\\ &\approx 1/2\ln M_{\text{Asym},+\boldsymbol{G}} - 1/2\ln M_{\text{Asym},-\boldsymbol{G}},\end{aligned} \tag{39}$$

rather than Eq. (17) by excluding the term $\chi_{0G\Delta^2}$ from $\ln M_{\text{Asym},+\boldsymbol{G}}$. Fig. 8 shows the validity of these assumptions.

6. Validity of the internal gradient ensemble model

The internal gradient distribution that we estimate with the proposed method is an effective gradient distribution resulting from the motional averaging of the spin-bearing particles [17]. The *internal*

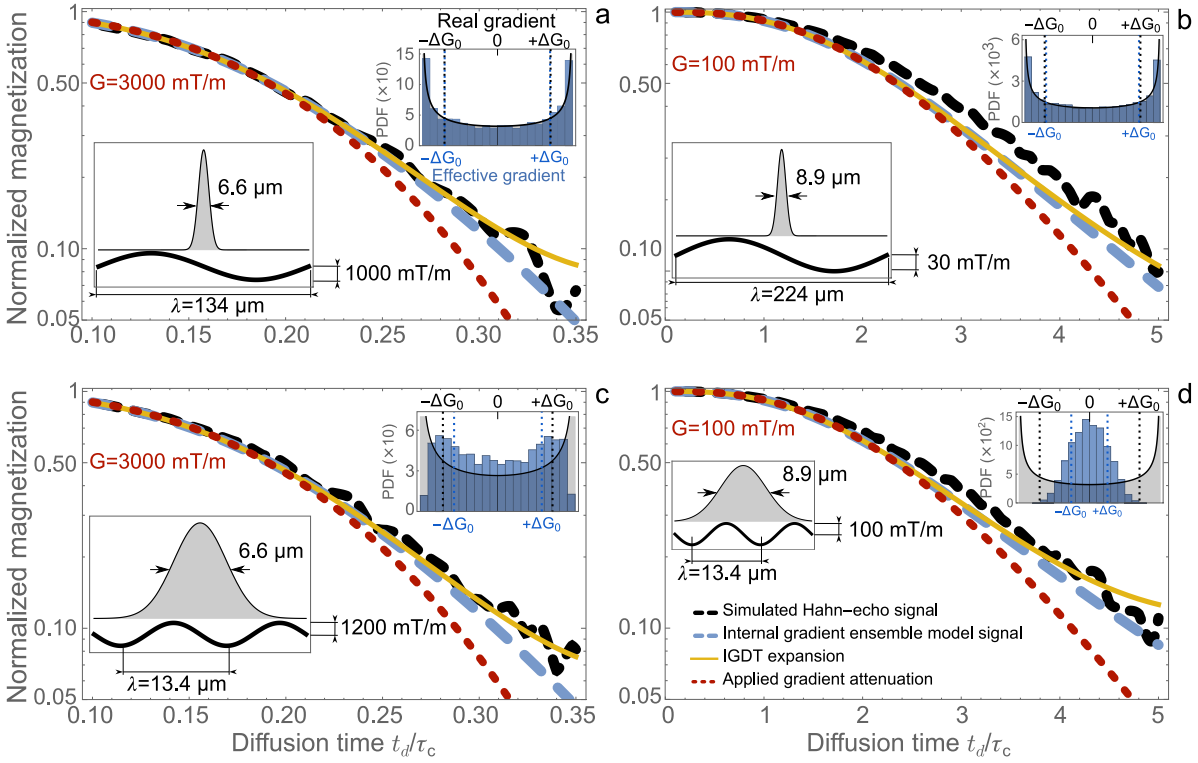

Fig. 9. Comparison of the predicted signal derived from the *internal gradient ensemble model* and the cumulant expansion framework with the exact signal of spin diffusing in a inhomogeneous magnetic field. Simulation of the magnetization decay of spin diffusion in an inhomogeneous magnetic field shown in the left inset of each panel in black solid line. The insets also show the relation between the background internal gradient wavelength and the diffusion length of the spin-bearing particles determined by the Gaussian distribution of the spin positions at the maximum diffusion times plotted in the main panels [t_d = 3.5 ms (a,c) and 50 ms (b,d) considering τ_c = 10 ms]. The insets on the right of each panel compare the real internal gradient distribution (black solid curve) with the effective one seen by the spins due to the motional averaging (blue histogram). Their corresponding standard deviations are shown with dashed vertical lines. The black dashed line in the main panels corresponds to the simulated magnetization for the considered spin-echo sequence of an ensemble of 5×10^3 spin-bearing particles driven by an OU process in presence of the sinusoidal background magnetic field gradient of wavelength λ and maximum internal gradient strength g. The blue dashed line corresponds to the magnetization averaged with the effective internal gradient distribution in the right insets using the *internal gradient ensemble model*. The red dotted line shows the signal decay only due to the spin interaction with the applied gradient. The yellow solid line is the signal decay derived from the IGDT-expansion of Eq. (34), evaluated with the moments of the effective gradient distribution of the right insets. The free diffusion coefficient is $D_0 = 2\,\mu m^2/ms$ and the diffusion correlation time $\tau_c = 10$ ms (associated with a restriction length $l_c = \sqrt{D_0\tau_c} = 4.47\,\mu m$). Four conditions are shown: (a) free diffusion regime with $\lambda = 30l_c$, $g = 1000$ mT/m and an applied gradient $G = 3000$ mT/m; (b) restricted diffusion regime with $\lambda = 50l_c$, $g = 30$ mT/m and $G = 100$ mT/m; (c) free diffusion regime with $\lambda = 3l_c$, $g = 1200$ mT/m and $G = 3000$ mT/m and (d) restricted diffusion regime with $\lambda = 3l_c$, $g = 100$ mT/m and $G = 100$ mT/m. (For interpretation of the references to color in this figure legend, the reader is referred to the web version of this article.)

gradient ensemble model implicitly simplifies the signal attenuation effects due to the spin movement in a space-dependent gradient field to the one induced by the spin movement in an effective constant internal gradient. Here, we evaluate the reliability of this assumption through the simulations of the magnetization decay of spin-bearing particles diffusing in a sinusoidal gradient field that models typical field inhomogenities in porous systems [25,65,103].

For this evaluation, we perform simulations in one spacial dimension by setting an applied gradient G and an inhomogeneous background magnetic field with a z-component

$$\Delta B_0(x) = g\frac{\lambda}{2\pi}\cos\left(\frac{2\pi}{\lambda}x\right), \tag{40}$$

where g is the maximum internal gradient strength and λ is the wavelength of the inhomogeneous internal field fluctuation. We consider four scenarios in Fig. 9, free and restricted diffusion regimes, where the internal magnetic field inhomogeneity wavelength λ is larger than and comparable to the diffusion restriction length l_c. We do not consider the case when the wavelength λ is shorter than the diffusion restriction length l_c, as the signal decay depends only on a averaged internal gradient value and the IGDT effect diminishes.

To focus on assessing the effects of internal gradient distributions and avoid misleading effects induced by the restriction complexity of the diffusion in a disordered medium, we simulate the diffusion process as an OU Gaussian process with a restriction length $l_c = \sqrt{D_0\tau_c}$. For the simulations, we evaluated 5000 stochastic realizations of the OU process with a mean spin-bearing particle position x_0 using a free diffusion coefficient $D_0 = 2\,\mu m^2/ms$ and a diffusion correlation time $\tau_c = 10$ ms. The mean particle position x_0 gives the barycenter of the confining cavity in a biological tissue or porous media. The initial particle position $x(0)$ is set equal to x_0 and it is randomly distributed within the spatial interval $(-\lambda, \lambda)$. We then calculate the spin magnetization signal of the diffusing spins in presence of the considered internal magnetic field inhomogeneity, together with a constant applied gradient with π-pulse at the diffusion time $t_d/2$ to provide a spin-echo modulation sequence.

The simulations are shown in Fig. 9 with black dashed curves. The blue dashed lines are the magnetization signal predicted by the *internal gradient ensemble model*. It is calculated using Eq. (36) and determined by the effective gradient distribution resulting from the motional averaging of the gradient explored by the spin from the beginning of the sequence up to the total diffusion time

$$G_0^i = \frac{1}{t_d}\int_0^{t_d} dt\,\frac{d}{dx}\Delta B_0\left(x_i\left(t\right)\right). \tag{41}$$

Here, the magnetic field shift $\Delta B_0(x)$ is given by Eq. (40), G_0^i is the effective internal gradient averaged by the ith spin-bearing particle along the $x_i(t)$ position trajectory. With the effective internal gradients G_0^i, we then generate a histogram as shown in blue in the insets of Fig. 9 compared with the real gradient distribution in black. The red dotted curves correspond to the magnetization decay only due to

the interaction with the applied gradient and the yellow solid lines correspond to the predicted signal derived from the IGDT-expansion of Eq. (34). In the four considered cases the expected signals derived from the cumulant expansion and *internal gradient ensemble model* are in good agreement with the simulated, exact one. Thus, this result shows that the effects in the magnetization decay of spin-bearing particles, diffusing in internal gradients that depend on its position, can be reduced to an effective internal gradient distribution based on an ensemble of gradients. Moreover, the magnetization signal decay is shown to be characterized only by the moments of the effective internal gradient distribution.

The presented simulations thus show the relevance and good signal prediction of the developed model to describe the complex diffusion process in presence of magnetic field inhomogenities induced by magnetic susceptibility heterogeneity in porous systems. Yet, we envisage some limitations. While the strength of the model is to reduce the complexity of the internal magnetic field heterogeneity to an *internal gradient ensemble model* characterized by the main moments of the distribution, it can only determine those moments and not the full internal gradient distribution. Then, different microstructure features might generate different distributions of internal gradients with similar first distribution moments. In those cases, the method cannot distinguish one distribution from the another. Moreover, the method is unable to provide information about multimodal gradient distributions, since that information is not encoded in the distribution moments. Further investigations should be made to identify which microstructures features can be identified with this method.

An important consideration evidenced by these results is that the molecular diffusion process can narrow the effective gradient distribution seen by the spins around its mean value as shown in Fig. 9d. Then, depending on the real gradient distribution variance, if the diffusion mean squared displacement is on the order of λ, the effective gradient variance may be much smaller than the real one or even the IGDT effects may vanish. While the predicted signal might be in agreement with the exact signal, as in Fig. 9d, some quantitative information about the real gradient field heterogeneities might be lost. However, while this still has to be strictly demonstrated, this limitation is probably a physical limitation due to the motional averaging induced by the diffusion process, and not due to our assumed model.

Another limitation is imposed by the time domain where the cumulant expansion is valid, defined by its convergence radius t_{conv} [73,104]. The cumulant expansion of Eq. (5) is valid for times shorter than its convergence radius, defined by $t_{conv} = |z|$ with z being the complex solution of $M(z) = 0$ and $M(z)$ the analytic continuation of Eq. (4) in the complex domain. Then, if the standard deviation of the internal gradient distribution is too high (for example > 500 mT/m in our simulations) the IGDT-expansion would be only valid at short times within the free diffusion regimen as shown in Fig. 9a and c.

7. Conclusions

Diffusion processes in disordered systems are of great interest in several areas as physics, biology and medicine, however they are very complex to characterize. In this article, we exploit the diffusion of spin-bearing particles to probe magnetic field inhomogenities that contain information about the media microstructure heterogeneities. We consider internal gradients induced by magnetic susceptibility heterogeneity that depend on the morphological information of the media. The spin-bearing particles diffuse within them and probe the effective gradients explored along their movement. We introduced a model that simplifies the naturally complex problem to an ensemble of spatially constant internal gradients that defines a distribution that can be characterized by its first moments. We demonstrate that this gradient ensemble approximation is useful as the gradients explored by the spin-bearing particles remains close to the real distribution in general, as in expected realistic conditions. We demonstrate that the diffusion process in an inhomogeneous field produces a motional average of the gradients seen by the spins, thus narrowing the effective internal gradient distribution. We also show that the spin magnetization decay is well characterized by only the moments of the effective internal gradient distribution.

This *internal gradient ensemble model* allows a spin phase's cumulant expansion decomposition for the magnetization signal decay. Based on this cumulant expansion framework, we derive an IGDT-expansion that provides the moments of the internal gradient distributions. The IGDT contain information about the anisotropies of the internal gradient distributions that intrinsically depend on the susceptibility heterogeneity of the media and its orientation with respect to the static magnetic field. Each IGDT term provides different information about the internal gradient distribution.

The IGDT effects may be weak in some scenarios, thus exploiting the presented framework, we propose modulated gradient spin echo sequences to enhance those effects. The enhancement strategy is based on smooth applied gradient modulations and a suitable timing interplay between the time modulating symmetries of the applied and internal gradients. We identify four groups of terms of the IGDT-expansion that can be measured independently by a suitable design of the pulse sequence using multiple applied gradient directions in a similar vein as DTI is estimated. We demonstrate the feasibility of the implementation of this framework to measure IGDT terms from the magnetization signal decay in free and restricted diffusion regimes using typical brain tissue conditions.

We also evaluate the validity of the model to represent the real distribution convoluted with the molecular diffusion process, and show the regimes where the model can be suitably used. We also discussed some limitations of the model. We observed that the effective internal gradient distribution reproduces well the real one when the diffusion is either free or the characteristic length of the internal gradients spatial variations is small compared with the diffusion length of the spin-bearing particles. However, in the restricted diffusion regime, the internal local gradients might be averaged by the molecular motion, thus losing information about their distribution. We thus expect the proposed IGDT method to be useful to monitor extra-axonal diffusion, since characteristic length might be wider than in the intra-axonal regions, thus allowing to extend the free diffusion time to probe smooth internal gradient variations [65].

As brain physiology is regulated by molecules and structures as the myelin sheath of axons with significant magnetic susceptibility in comparison with the surrounding medium, the degree of axon myelination significantly affects the internal gradient distributions [22,23,65,101]. Thus internal gradient distributions show correlations with the amount of myelin in tissues as potential biomarkers for many degenerative diseases. Our results thus contribute to estimate IGDT in this situations that may be especially useful for unveiling structures and fiber orientation based on these susceptibility induced changes [49,63–65]. The IGDT are complementary to DTI as they may estimate anisotropies when diffusion is free or isotropic.

Declaration of competing interest

The authors declare that they have no known competing financial interests or personal relationships that could have appeared to influence the work reported in this paper.

Data availability

Data will be made available on request.

Acknowledgments

We thank Melisa Gimenez and Martin Kuffer for reading the article and for their suggestions to improve the writing, and to Manuel O. Caceres for the fruitful discussions. This work was supported by CNEA; CONICET; ANPCyT-FONCyT PICT-2017-3156, PICT-2017-3699, PICT-2018-4333, PICT-2021-GRF-TI-00134, PICT-2021-I-A-00070; PIP-CONICET (11220170100486CO); UNCUYO SIIP Tipo I 2019-C028, 2022-C002, 2022-C030; Instituto Balseiro, Argentina; Collaboration programs between the MINCyT (Argentina), and MAECI (Italy) and MOST (Israel), and Erasmus+ Higher Education program from the European Commission between the CIMEC (University of Trento) and the Instituto Balseiro (Universidad Nacional de Cuyo).

Appendix A. Analysis of the effective gradient assumptions

In this Appendix, we evaluate the approximation of Eq. (1) with Eq. (3) in the main text for the considered *internal gradient ensemble model* (Section 2.2). We here focus only on the internal field gradient contribution in Eqs. (3) and (1) in one dimension. Thus, the cornerstone approximation is

$$\phi(t) = \int_0^t dt' f(t') \Delta B_0 \left[\boldsymbol{x}(t')\right] \approx \int_0^t dt' f(t') G_0 x(t'), \tag{A.1}$$

where we assume that the spin phase accumulation is induced by an effective and spatially constant internal field gradient G_0 that is probed by the spin during the diffusion time t_d [17].

We assess the effects on the MR signal of the next order correction to the approximation of Eq. (A.1). Without loss of generality, we assume that $\langle x(t)\rangle = 0$ and $\langle G_0(x)\rangle = 0$. Then, the second cumulant of the accumulated spin-phase is

$$\left\langle\left\langle \phi^2(t)\right\rangle\right\rangle = \int_0^t dt_1 \int_0^t dt_2 f(t_1) f(t_2) \langle G_0(x_1) G_0(x_2) x_1 x_2\rangle_{G_0,x}, \tag{A.2}$$

where we consider the internal gradient depends on the spatial position. Here we define $x_i \equiv x(t_i)$ and $f(t)$ is a MGSE modulation such that $\int_0^t dt' f(t') = 0$ as described in the main text. Eq. (A.2) includes the average over the disorder of the internal gradient $G_0(x)$ and the one induced by the thermal fluctuation of the spin position $x(t)$.

We assume that the thermal stochastic process is independent of the disorder of $G_0(x)$. Then, we can first apply the average over the $G_0(x)$ realizations. This assumption is an approximation, as the structures within the medium that hinder the free diffusion, also serve as sources of internal gradients. However, particle diffusion is locally affected by the structures in its surroundings, while internal gradients at a given spatial position are generated by many more and more distant structures. Then, there is plausibly a weak correlation between gradient and particle position, making it possible to factorize their joint probability density function. Based on this considerations, we consider an exponential correlation for the disorder as a function of the spatial distance between two spin positions, *i.e.*

$$\langle G_0(x_1) G_0(x_2)\rangle_{G_0} = \left\langle G_0^2\right\rangle e^{-\frac{|x_1 - x_2|}{\lambda}}. \tag{A.3}$$

The *internal gradient ensemble model* assumption of considering that the diffusing particles feel an effective constant gradient is exact in the limit of $\lambda \to \infty$. Then, the first order correction to the correlation function (A.3) is

$$\langle G_0(x_1) G_0(x_2)\rangle_{G_0} \approx \left\langle G_0^2\right\rangle \left(1 - \frac{|x_1 - x_2|}{\lambda}\right).$$

Considering that $x(t)$ fluctuates by an Ornstein–Uhlenbeck (OU) process, the self-correlation function is $\langle x_1 x_2\rangle = l_c^2 e^{-\frac{\Delta t}{\tau_c}}$ with $\Delta t = |t_1 - t_2|$ and $l_c^2 = D_0 \tau_c$ the correlation length of the diffusion process. The correlator in Eq. (A.2) becomes

$$\langle G_0(x_1) G_0(x_2) x_1 x_2\rangle_{G_0,x}$$

$$\approx \left\langle G_0^2\right\rangle \left(l_c^2 e^{-\frac{\Delta t}{\tau_c}} - \frac{\langle |x_1 - x_2| x_1 x_2\rangle}{\lambda}\right),$$

where the first term in the right hand side is the self-correlation function of the spin position and the second one is the first order correction by the internal gradient disorder correlation. The average $\langle |x_1 - x_2| x_1 x_2\rangle$ over the OU paths results

$$\langle |x_1 - x_2| x_1 x_2\rangle = \frac{l_c^3 \sqrt{1 - e^{-\Delta t/\tau_c}} \left(3e^{-\Delta t/\tau_c} - 1\right)}{\sqrt{\pi}},$$

and at long Δt times with respect to the correlation time τ_c gives a constant

$$\langle |x_1 - x_2| x_1 x_2\rangle \overset{\Delta t \gg \tau_c}{\longrightarrow} -\frac{l_c^3}{\sqrt{\pi}} = \text{const.}$$

On the other hand, at short Δt times

$$\langle |x_1 - x_2| x_1 x_2\rangle \overset{\Delta t \ll \tau_c}{\longrightarrow} \frac{2 l_c^3}{\sqrt{\pi}} \sqrt{\Delta t/\tau_c}.$$

Yet we can calculate numerically the correlator $\langle G_0(x_1) G_0(x_2) x_1 x_2\rangle_{G_0,x}$ using the exponential model of Eq. (A.3) and observe the same behavior at long and short times, *i.e.* a constant value at long times $\Delta t \gg \tau_c$ and $l_c^2(1 - \frac{\Delta t}{\tau_c}) - \frac{2 l_c^3}{\lambda\sqrt{\pi}} \sqrt{\Delta t/\tau_c}$ at short times $\Delta t \ll \tau_c$. Integrating Eq. (A.2), then we find that at short times the internal gradient disorder contribution $\propto \frac{l_c^3}{\lambda} \left(\frac{t}{\tau_c}\right)^{5/2}$ is a small correction to the contribution of the thermal fluctuation of position that varies as $l_c^2 \left(\frac{t}{\tau_c}\right)^3$. At long times, as the disorder correction becomes constant and MGSE gives $\int_0^t dt' f(t') = 0$, its contribution is null and the magnetization decay is just driven by the thermal fluctuation of position. Then, this demonstrate that for λ much larger than the diffusion length, the approximation of Eq. (A.1) is valid.

In this work, we also shown that the approximation of Eq. (A.1) holds even if the diffusion length is comparable or larger than λ (see Fig. 9 in the main text). We here analyze the extreme limit of $\lambda \to 0$ in the long time limit. Eq. (A.3) can be then approximated with a Dirac delta function as

$$\langle G_0(x_1) G_0(x_2)\rangle_{G_0} \approx 2\lambda \left\langle G_0^2\right\rangle \delta(x_1 - x_2).$$

Then the average over the OU paths gives

$$\langle G_0(x_1) G_0(x_2) x_1 x_2\rangle_{G_0,x} \approx \frac{\lambda l_c \left\langle G_0^2\right\rangle}{\sqrt{2\pi}} \frac{\cosh\left(\frac{\Delta t}{2\tau_c}\right)}{\sqrt{e^{\Delta t/\tau_c} - 1}}.$$

The long time limit of this correlator gives

$$\langle G_0(x_1) G_0(x_2) x_1 x_2\rangle_{G_0,x} \overset{\Delta t \gg \tau_c}{\longrightarrow} \frac{\lambda l_c \left\langle G_0^2\right\rangle}{2\sqrt{2\pi}} \left(1 + e^{-\Delta t/\tau_c}\right). \tag{A.4}$$

The right hand side of Eq. (A.4) has two terms, the first one is a constant and thus does not contribute to the integral of Eq. (A.2) as $\int_0^t dt' f(t') = 0$. Only the second term contributes to the integral, and it is proportional to the thermal fluctuation correlation of the spin position $\langle x_1 x_2\rangle$, *i.e.* $\frac{\lambda\left\langle G_0^2\right\rangle}{2 l_c \sqrt{2\pi}} \langle x_1 x_2\rangle$. This term thus drives the magnetization decay at long times in accordance with our approximation (A.1) except for the proportionality constant $\frac{\lambda}{2 l_c \sqrt{2\pi}}$. This shows that the variance of the effective internal gradient reduces with reducing λ. This is consistent with the assumption of the effective internal gradient distribution resulting from the motional average of the spin-bearing particles. The variance of the distribution reduces as the particles explore their environment in accordance with the discussion in Section 6.

This analysis and the validity of the approximation (A.1) are consistent with the Effective Medium Theory (EMT) [54]. The effects on the MR signal due to the disorder of the internal gradient $G_0(x)$ could be interpreted in terms of an effective medium that gives an effective

internal gradient as a function of time $G_0(t)$. In Ref. [54], the apparent diffusion coefficient is given by a correction to the free diffusion coefficient D_0, determined by considering a Brownian diffusion process and disorder in the Larmor frequency of the spins. This is equivalent to the disordered internal field $G_0(x)$ considered in this work. In our model assumptions, the diffusion coefficient is always accompanied by the variance of the internal gradient $\langle G_0^2 \rangle$ in a given spin position. The correction derived in [54] can be thus interpreted either on D_0 or on $\langle G_0^2 \rangle$. The authors in Ref. [54] obtain an universal correction for D_0 that diverges as a power law at long times $D^{\text{app}} - D_0 \sim -t^{2-d/2}$, that depends on the space dimension d and D^{app} is the apparent diffusion coefficient. This results is consistent with our assumption of an effective internal gradient resulting from the motional average of the spin position. Based on this considerations, we expect that $\langle G_0^2(t) \rangle$ decreases with time as the spin-bearing particles explore more and more gradient strengths along their trajectory. A more rigorously demonstration of our assumptions based on this approach, would need the EMT corrections for $\langle G_0^2 \rangle$ in the context of an OU diffusion process. In this work, we made Monte Carlo simulations assuming a reasonable ansatz for the effective internal gradient based on Eq. (41) to show the validity of the approximation.

Appendix B. General demonstration of the proposed sequence design conditions defines $|\boldsymbol{\beta}^{0G}(t_d)| - \boldsymbol{\beta}^{GG}(t_d)$ positive-definite

We show in Section 4.2 of the main text, a necessary relation between the overlap matrices $\boldsymbol{\beta}^{GG}$ and $\boldsymbol{\beta}^{0G}$ that have to be fulfilled for enhancing the cross term contributions in Eq. (16). Thus the relation we derive is a necessary condition, since there are other factors that control the intensity of these terms such as the angle between the applied and mean background gradient or even the applied gradient strength. Considering the first two terms $\frac{1}{2} G_i \beta_{ij}^{GG}(t) G_j$ and $G_i \beta_{ij}^{0G}(t) \langle \boldsymbol{G}_0 \rangle_j$ in Eq. (16), we require

$$\left| \boldsymbol{n} \cdot \boldsymbol{\beta}^{0G} \cdot \boldsymbol{n} \right| > \boldsymbol{n} \cdot \boldsymbol{\beta}^{GG} \cdot \boldsymbol{n} \tag{B.1}$$

for the matrix elements in an arbitrary n direction, to enhance the weight of the second term compared to the first one. We thus focus on the maximization of the cross terms overlap matrices $\boldsymbol{\beta}^{0G}$. In the principal axes of the matrices $\boldsymbol{\beta}^{GG}$ and $\boldsymbol{\beta}^{0G}$, the matrix element can be written as

$$\left| n \cdot \boldsymbol{\beta}^{0G} \cdot n \right| = \left| \sum_j \left(\tilde{n}_j \right)^2 \beta_j^{0G} \right| \leq \sum_j \left(\tilde{n}_j \right)^2 \left| \beta_j^{0G} \right|,$$

where $\tilde{n}_j$ are the components of the unit vector $\boldsymbol{n}$ in the overlap matrices eigenbasis. Thus requiring the condition $n \cdot \left| \boldsymbol{\beta}^{0G} \right| \cdot n > n \cdot \boldsymbol{\beta}^{GG} \cdot n$ is equivalent to request $|\boldsymbol{\beta}^{0G}(t_d)| - \boldsymbol{\beta}^{GG}(t_d)$ to be positive-definite.

In Section 4.2, we derived general conditions that the gradient control sequences have to fulfill in order to satisfy (21). That is: (*i*) the background gradient modulation $f_0(t)$ has to be an even function with respect to $t_d/2$ with a minimal number of pulses; (*ii*) the applied gradient modulation has to be an MGSE sequence with a smooth modulation function ($|f_G(t)| \leq 1$), with a single refocusing echo matching the zero crossing time with a π-pulse that modulate $f_0(t)$ and (*iii*) the modulation function $f_G(t)$ has to be an odd function with respect to its middle time, *i.e.* the zero crossing time, and should vanish also at every π-pulse that modulate $f_0(t)$. These conditions ensure that the effective interaction times defined in Eqs. (23) and (24) satisfy $T_{0G} > T_G$. Moreover, if ω_0 is the frequency at the highest pick of the cross modulation filter and ω_G the frequency at the maximum applied gradient filter, the above conditions also ensure $\omega_G > \omega_0$.

The filters in the overlap integrals in Eqs. (8) and (10) have a bandwidth around the frequencies ω_G and ω_0, respectively. If the filter bandwidths are small compared with the spectral density width, we can factor out from the integral the noise spectral density at the filter frequency, since it is approximately constant within the filter bandwidth. Then, Eqs. (8) and (10) can be approximated by $\boldsymbol{\beta}^{GG}(t_d) \approx \gamma^2 \boldsymbol{S}(\omega_G) T_G$ and $\boldsymbol{\beta}^{0G}(t_d) \approx \gamma^2 \boldsymbol{S}(\omega_0) T_{0G}$, respectively. If not, we can roughly hold this approximation, since we can take the constant $\boldsymbol{S}(\omega^*)$ out from the integral, with ω^* belonging to the filter bandwidth and $\omega^* \approx \omega_G$ and $\omega^* \approx \omega_0$ respectively. Here, the diffusion time t_d dependence is encoded in the effective interactions times and gradient modulation frequencies. Generally, the eigenvalues $S(\omega)$ of the spectral density are monotonically decreasing functions of ω with a maximum at zero frequency. Then, since $\omega_G > \omega_0$ and $T_{0G} > T_G$, $|\boldsymbol{\beta}^{0G}(t_d)| - \boldsymbol{\beta}^{GG}(t_d)$ is positive-definite.

Appendix C. Enhancing the cross-filter overlap with the diffusion spectral density

In Section 4.2, we derive the conditions that gradient modulation sequences have to fulfill to guarantee the matrix $|\boldsymbol{\beta}^{0G}(t_d)| - \boldsymbol{\beta}^{GG}(t_d)$ to be positive-definite. This condition is ensured by making the effective interaction times of gradients with the diffusing spin-bearing particles defined in Eqs. ((23), (24)) to satisfy $T_{0G} > T_G$. This condition is achieved by making $f_0(t) f_G(t) = |f_G(t)|$.

We thus aim to maximize the eigenvalues of the matrix $|\boldsymbol{\beta}^{0G}(t_d)| - \boldsymbol{\beta}^{GG}(t_d)$. For that, we maximize the lowest frequency peak of the cross-filter $\Re \left[F_0(\omega, t_d) F_G^*(\omega, t_d) \right]$. In principle, the condition $f_0(t) f_G(t) = |f_G(t)|$ and the maximization of the low frequency peak of the cross-filter are independents, and might not be satisfied simultaneously. Here we demonstrate that, in fact, both condition could be satisfied at the same time.

First we evaluate the condition for the time-shift of the applied gradient modulation for the asymmetric sequence that maximize *the cross-term* overlap contribution. This time-shift maximizes the cross-filter at the background gradient modulation frequency in order to optimize the overlap with the displacement spectral density $\boldsymbol{S}(\omega)$. The cross-filter can be written as

$$\Re \left[F_0(\omega) F_G^*(\omega) \right] = \widetilde{F}_0(\omega) \widetilde{F}_G(\omega) \cos \left[\omega \Delta t - \pi/2 \right] \tag{C.1}$$

assuming an arbitrary time-shift Δt, where $\widetilde{F}_0(\omega)$ and $\widetilde{F}_G(\omega)$ are real functions corresponding to the Fourier transform of the gradient modulations centered at $t = 0$. The phase shift in $\pi/2$ comes from the fact that we consider the applied gradient modulation as an odd function. Here we omit the diffusion time t_d dependence of the Fourier transform in order to simplify the notation. Let be ω_0 the principal harmonic frequency of the background gradient modulation $f_0(t)$. For the two pulse CPMG sequence, the main harmonic is $\omega_0 \approx 2\pi/t_d$. To optimize the cross-filter of Eq. (C.1), we require that

$$\omega_0 \Delta t - \pi/2 = n\pi$$

with $|n| = 0, 1, 2....$ Then, the optimal time-shift is

$$\Delta t = \frac{\pi}{\omega_0}(n + 1/2). \tag{C.2}$$

There are two solution with n such that $\Delta t < t_d/2$ which give $\Delta t = \pm t_d/4$. These time shifts synchronize exactly the zero crossing time of $f_G(t)$ with the times when the RF π-pulse are applied in the two pulse CPMG sequence.

This optimization is useful as long as $|\widetilde{F}_0(\omega_0)| > |\widetilde{F}_G(\omega_0)| > 0$. The first relation is always true by construction and the second one impose a restriction on how high can be the frequency with which can be modulated the applied gradient. Thus we show how both requirements to enhance the background gradient effect, the effective interaction times relation $T_{0G} > T_G$ and the low frequency filtering of the cross modulation, can be optimized simultaneously.

$$\beta^{0G}(t_d) = \gamma^2 D_0 \sqrt{\frac{\pi e}{2}} \tau_c \alpha^2 t_d^2 e^{\frac{\alpha^2 t_d^2}{2\tau_c^2}} \left[4\mathrm{erfc}\left(\frac{\alpha t_d}{\sqrt{2}\tau_c}\right) - 2e^{\frac{t_d}{2\tau_c}} \mathrm{erfc}\left(\frac{\alpha t_d/\tau_c + 1/(2\alpha)}{\sqrt{2}}\right) - 2e^{-\frac{T}{2\tau}} \mathrm{erfc}\left(\frac{\alpha t_d/\tau_c - 1/(2\alpha)}{\sqrt{2}}\right) - e^{\frac{t_d}{4\tau_c}} \mathrm{erfc}\left(\frac{\alpha T/\tau_c + 1/(4\alpha)}{\sqrt{2}}\right) - e^{-\frac{t_d}{4\tau_c}} \mathrm{erfc}\left(\frac{\alpha t_d/\tau_c - 1/(4\alpha)}{\sqrt{2}}\right) + e^{\frac{3t_d}{4\tau_c}} \mathrm{erfc}\left(\frac{\alpha t_d/\tau_c + 3/(4\alpha)}{\sqrt{2}}\right) + e^{-\frac{3t_d}{4\tau_c}} \mathrm{erfc}\left(\frac{\alpha t_d/\tau_c - 3/(4\alpha)}{\sqrt{2}}\right) \right]. \quad \text{(D.7)}$$

Box II.

Appendix D. General filters and overlap functions

In this section we provide the exact expression for the filters of the GDGSE modulation, a two-pulses CPMG sequence modulation, and the cross filter $\Re\left[F_0(\omega,t_d)F_G^*(\omega,t_d)\right]$ that appear in Eqs. (8)–(10) in the main text. We consider the gradients modulations independent of the applied gradient direction. We also provide the exact analytic expressions for the corresponding overlap functions for one dimensional diffusion. The filter function for the two pulse CPMG sequence of the background gradient modulation is

$$|F_0(\omega,t_d)|^2 = \frac{256}{\omega^2}\cos^2\left(\frac{t_d\omega}{8}\right)\sin^6\left(\frac{t_d\omega}{8}\right). \quad \text{(D.1)}$$

The Fourier transform of the GDGSE modulation is

$$F_G(\omega,t_d) = i\sqrt{2\pi e}\alpha^2 t_d^2 \omega e^{i\frac{T}{2}\omega} e^{-\frac{\alpha^2 t_d^2}{2}\omega^2} \quad \text{(D.2)}$$

and thus its filter function is

$$|F_G(\omega,t_d)|^2 = 2\pi e\alpha^4 t_d^4 \omega^2 e^{-\alpha^2 t_d^2 \omega^2}. \quad \text{(D.3)}$$

The cross-filter is

$$\Re\left[F_0(\omega,t_d)F_G^*(\omega,t_d)\right] = 32\sqrt{2\pi e}\alpha^2 t_d^2 e^{-\frac{\alpha^2 t_d^2}{2}\omega^2} \times \cos^2\left(\frac{t_d\omega}{8}\right)\sin^4\left(\frac{t_d\omega}{8}\right). \quad \text{(D.4)}$$

With these filters and considering the diffusion spectral density

$$S(\omega) = 2D_0\left(\tau_c^{-2} + \omega^2\right)^{-1},$$

we determine the overlap functions using Eqs. (8)–(10) in the main text

$$\beta^{GG}(t_d) = 2\gamma^2 D_0 \sqrt{\pi e}\alpha^3 t_d^3 \left[1 - \frac{\sqrt{\pi}\alpha t_d}{\tau_c} e^{\frac{\alpha^2 t_d^2}{\tau_c^2}} \mathrm{erfc}\left(\frac{\alpha t_d}{\tau_c}\right)\right], \quad \text{(D.5)}$$

$$\beta^{00}(t_d) = 2\gamma^2 D_0 \tau_c^3 \left(\frac{t_d}{\tau_c} - 5 + e^{-\frac{t_d}{\tau_c}} - 4e^{-\frac{3t_d}{4\tau_c}} + 4e^{-\frac{t_d}{2\tau_c}} + 4e^{-\frac{t_d}{4\tau_c}}\right), \quad \text{(D.6)}$$

and (see Eq. (D.7) given in Box II). Here, $\mathrm{erfc}(x)$ denote the complementary error function. The generalization to a three-dimensional diffusion is made by considering the correlation time τ_c as a rank 3 tensor, whose eigenvalues are the correlation times in its principal directions, as is shown in Fig. 3 of the main text.

References

[1] D.S. Grebenkov, NMR survey of reflected Brownian motion, Rev. Modern Phys. 79 (2007) 1077, http://dx.doi.org/10.1103/RevModPhys.79.1077.

[2] M. Palombo, C. Ligneul, C. Najac, J.L. Douce, J. Flament, C. Escartin, P. Hantraye, E. Brouillet, G. Bonvento, J. Valette, New paradigm to assess brain cell morphology by diffusion-weighted MR spectroscopy in vivo, Proc. Natl. Acad. Sci. USA 113 (24) (2016) 6671–6676, http://dx.doi.org/10.1073/pnas.1504327113.

[3] L. Latour, R. Kleinberg, P. Mitra, C. Sotak, Pore-size distributions and tortuosity in heterogeneous porous media, J. Magn. Reson. A 112 (1) (1995) 83–91, http://dx.doi.org/10.1006/jmra.1995.1012.

[4] K.R. Brownstein, C.E. Tarr, Importance of classical diffusion in NMR studies of water in biological cells, Phys. Rev. A 19 (6) (1979) 2446–2453, http://dx.doi.org/10.1103/physreva.19.2446.

[5] M.E. Komlosh, E. Özarslan, M.J. Lizak, F. Horkay, V. Schram, N. Shemesh, Y. Cohen, P.J. Basser, Pore diameter mapping using double pulsed-field gradient MRI and its validation using a novel glass capillary array phantom, J. Magn. Reson. 208 (1) (2011) 128–135, http://dx.doi.org/10.1016/j.jmr.2010.10.014.

[6] I. Drobnjak, H. Zhang, A. Ianuş, E. Kaden, D.C. Alexander, PGSE, OGSE, and sensitivity to axon diameter in diffusion MRI: Insight from a simulation study, Magn. Reson. Med. 75 (2) (2015) 688–700, http://dx.doi.org/10.1002/mrm.25631.

[7] M. Nilsson, S. Lasič, I. Drobnjak, D. Topgaard, C.-F. Westin, Resolution limit of cylinder diameter estimation by diffusion MRI: The impact of gradient waveform and orientation dispersion, NMR Biomed. 30 (7) (2017) e3711, http://dx.doi.org/10.1002/nbm.3711.

[8] J. Xu, X. Jiang, H. Li, L.R. Arlinghaus, E.T. McKinley, S.P. Devan, B.M. Hardy, J. Xie, H. Kang, A.B. Chakravarthy, J.C. Gore, Magnetic resonance imaging of mean cell size in human breast tumors, Magn. Reson. Med. 83 (6) (2019) 2002–2014, http://dx.doi.org/10.1002/mrm.28056.

[9] J. Veraart, D. Nunes, U. Rudrapatna, E. Fieremans, D.K. Jones, D.S. Novikov, N. Shemesh, Noninvasive quantification of axon radii using diffusion MRI, eLife 9 (2020) e49855, http://dx.doi.org/10.7554/elife.49855.

[10] Y. Assaf, T. Blumenfeld-Katzir, Y. Yovel, P.J. Basser, AxCaliber: a method for measuring axon diameter distribution from diffusion MRI, Magn. Reson. Med. 59 (6) (2008) 1347–1354, http://dx.doi.org/10.1002/mrm.21577.

[11] J.C. Gore, J. Xu, D.C. Colvin, T.E. Yankeelov, E.C. Parsons, M.D. Does, Characterization of tissue structure at varying length scales using temporal diffusion spectroscopy, NMR Biomed. 23 (7) (2010) 745, http://dx.doi.org/10.1002/nbm.1531.

[12] N. Shemesh, G.A. Álvarez, L. Frydman, Size distribution imaging by non-uniform oscillating-gradient spin echo (NOGSE) MRI, PLoS One 10 (7) (2015) e0133201, http://dx.doi.org/10.1371/journal.pone.0133201.

[13] M. Capiglioni, A. Zwick, P. Jiménez, G.A. Álvarez, Noninvasive quantitative imaging of selective microstructure sizes via magnetic resonance, Phys. Rev. Appl. 15 (2021) 014045, http://dx.doi.org/10.1103/PhysRevApplied.15.014045.

[14] H.H. Ong, F.W. Wehrli, Quantifying axon diameter and intra-cellular volume fraction in excised mouse spinal cord with q-space imaging, NeuroImage 51 (4) (2010) 1360–1366, http://dx.doi.org/10.1016/j.neuroimage.2010.03.063.

[15] J. Xu, H. Li, K.D. Harkins, X. Jiang, J. Xie, H. Kang, M.D. Does, J.C. Gore, Mapping mean axon diameter and axonal volume fraction by MRI using temporal diffusion spectroscopy, Neuroimage 103 (2014) 10–19, http://dx.doi.org/10.1016/j.neuroimage.2014.09.006.

[16] D. Ludwig, F.B. Laun, K.D. Klika, J. Rauch, M.E. Ladd, P. Bachert, T.A. Kuder, Diffusion pore imaging in the presence of extraporal water, J. Magn. Reson. 339 (2022) 107219, http://dx.doi.org/10.1016/j.jmr.2022.107219.

[17] M.D. Hürlimann, Effective gradients in porous media due to susceptibility differences, J. Magn. Reson. 131 (2) (1998) 232–240, http://dx.doi.org/10.1006/jmre.1998.1364.

[18] P.N. Sen, S. Axelrod, Inhomogeneity in local magnetic field due to susceptibility contrast, J. Appl. Phys. 86 (8) (1999) 4548, http://dx.doi.org/10.1063/1.371401.

[19] Y.-Q. Song, Determining pore sizes using an internal magnetic field, J. Magn. Reson. 143 (2) (2000) 397–401, http://dx.doi.org/10.1006/jmre.1999.2012.

[20] S. Wharton, R. Bowtell, Whole-brain susceptibility mapping at high field: A comparison of multiple- and single-orientation methods, Neuroimage 53 (2) (2010) 515, http://dx.doi.org/10.1016/j.neuroimage.2010.06.070.

[21] L. de Rochefort, T. Liu, B. Kressler, J. Liu, P. Spincemaille, V. Lebon, J. Wu, Y. Wang, Quantitative susceptibility map reconstruction from MR phase data using bayesian regularization: Validation and application to brain imaging, Magn. Reson. Med. 63 (1) (2010) 194, http://dx.doi.org/10.1002/mrm.22187.

[22] C. Liu, W. Li, G.A. Johnson, B. Wu, High-field (9.4T) MRI of brain dysmyelination by quantitative mapping of magnetic susceptibility, Neuroimage 56 (3) (2011) 930–938, http://dx.doi.org/10.1016/j.neuroimage.2011.02.024.

[23] J. Lee, K. Shmueli, B.-T. Kang, B. Yao, M. Fukunaga, P. van Gelderen, S. Palumbo, F. Bosetti, A.C. Silva, J.H. Duyn, The contribution of myelin to magnetic susceptibility-weighted contrasts in high-field MRI of the brain, Neuroimage 59 (4) (2012) 3967–3975, http://dx.doi.org/10.1016/j.neuroimage.2011.10.076.

[24] W. Li, B. Wu, A.V. Avram, C. Liu, Magnetic susceptibility anisotropy of human brain in vivo and its molecular underpinnings, Neuroimage 59 (3) (2012) 2088, http://dx.doi.org/10.1016/j.neuroimage.2011.10.038.

[25] P.T. Callaghan, Translational Dynamics and Magnetic Resonance: Principles of Pulsed Gradient Spin Echo NMR, OUP Oxford, 2011.

[26] M. Drake-Pérez, J. Boto, A. Fitsiori, K. Lovblad, M.I. Vargas, Clinical applications of diffusion weighted imaging in neuroradiology, Insights Imaging 9 (4) (2018) 535–547, http://dx.doi.org/10.1007/s13244-018-0624-3.

[27] C. Messina, R. Bignone, A. Bruno, A. Bruno, F. Bruno, M. Calandri, D. Caruso, P. Coppolino, R.D. Robertis, F. Gentili, I. Grazzini, R. Natella, P. Scalise, A. Barile, R. Grassi, D. Albano, Diffusion-weighted imaging in oncology: An update, Cancers 12 (6) (2020) 1493, http://dx.doi.org/10.3390/cancers12061493.

[28] P.J. Basser, J. Mattiello, D.L. Bihan, Estimation of the effective self-diffusion tensor from the NMR spin echo, J. Magn. Reson. B 103 (3) (1994) 247, http://dx.doi.org/10.1006/jmrb.1994.1037.

[29] P.J. Basser, J. Mattiello, D.L. Bihan, MR diffusion tensor spectroscopy and imaging, Biophys. J. 66 (1) (1994) 259, http://dx.doi.org/10.1016/S0006-3495(94)80775-1.

[30] S. Mori, B.J. Crain, V.P. Chacko, P.C.M. Van Zijl, Three-dimensional tracking of axonal projections in the brain by magnetic resonance imaging, Ann. Neurol. 45 (2) (1999) 265–269, http://dx.doi.org/10.1002/1531-8249(199902)45:2<265::AID-ANA21>3.0.CO;2-3.

[31] D. Le Bihan, J.-F. Mangin, C. Poupon, C.A. Clark, S. Pappata, N. Molko, H. Chabriat, Diffusion tensor imaging: concepts and applications, J. Magn. Reson. Imaging 13 (4) (2001) 534–546, http://dx.doi.org/10.1002/jmri.1076.

[32] K.W. Andersen, S. Lasič, H. Lundell, M. Nilsson, D. Topgaard, F. Sellebjerg, F. Szczepankiewicz, H.R. Siebner, M. Blinkenberg, T.B. Dyrby, Disentangling white-matter damage from physiological fibre orientation dispersion in multiple sclerosis, Brain Commun. 2 (2) (2020) fcaa077, http://dx.doi.org/10.1093/braincomms/fcaa077.

[33] P.J. Basser, D.K. Jones, Diffusion-tensor MRI: theory, experimental design and data analysis – a technical review, NMR Biomed. 15 (7–8) (2002) 456–467, http://dx.doi.org/10.1002/nbm.783.

[34] S. Mori, P.C.M. van Zijl, Fiber tracking: principles and strategies – a technical review, NMR Biomed. 15 (7–8) (2002) 468–480, http://dx.doi.org/10.1002/nbm.781.

[35] J. Duyn, MR susceptibility imaging, J. Magn. Reson. 229 (2013) 198–207, http://dx.doi.org/10.1016/j.jmr.2012.11.013.

[36] E. Haacke, J. Patrick, G. Lenz, T. Parrish, The separation of water and lipid components in the presence of field inhomogeneities, Rev. Magn. Reson. Med. 1 (2) (1986) 123–154.

[37] J. Mao, H. Yan, W. Brey, W. Bidgood, J. Steinbach, A. Mancuso, Fat tissue and fat suppression, Magn. Reson. Imaging 11 (3) (1993) 385–393, http://dx.doi.org/10.1016/0730-725x(93)90071-k.

[38] L. Axel, Blood flow effects in magnetic resonance imaging, Magn. Reson. Annu. (1986) 237–244.

[39] R. Alfidi, T. Masaryk, E. Haacke, G. Lenz, J. Ross, M. Modic, A. Nelson, J. LiPuma, A. Cohen, MR angiography of peripheral, carotid, and coronary arteries, Am. J. Roentgenol. 149 (6) (1987) 1097–1109, http://dx.doi.org/10.2214/ajr.149.6.1097.

[40] J.R. Reichenbach, R. Venkatesan, D.J. Schillinger, D.K. Kido, E.M. Haacke, Small vessels in the human brain: MR venography with deoxyhemoglobin as an intrinsic contrast agent, Radiology 204 (1) (1997) 272–277, http://dx.doi.org/10.1148/radiology.204.1.9205259.

[41] J.H. Duyn, P. van Gelderen, T.-Q. Li, J.A. de Zwart, A.P. Koretsky, M. Fukunaga, High-field MRI of brain cortical substructure based on signal phase, Proc. Natl. Acad. Sci. 104 (28) (2007) 11796–11801, http://dx.doi.org/10.1073/pnas.0610821104.

[42] S. Eskreis-Winkler, K. Deh, A. Gupta, T. Liu, C. Wisnieff, M. Jin, S.A. Gauthier, Y. Wang, P. Spincemaille, Multiple sclerosis lesion geometry in quantitative susceptibility mapping (QSM) and phase imaging, J. Magn. Reson. Imaging 42 (1) (2014) 224–229, http://dx.doi.org/10.1002/jmri.24745.

[43] S. Eskreis-Winkler, Y. Zhang, J. Zhang, Z. Liu, A. Dimov, A. Gupta, Y. Wang, The clinical utility of QSM: disease diagnosis, medical management, and surgical planning, NMR Biomed. 30 (4) (2016) e3668, http://dx.doi.org/10.1002/nbm.3668.

[44] C. Wang, A.B. Martins-Bach, F. Alfaro-Almagro, G. Douaud, J.C. Klein, A. Llera, C. Fiscone, R. Bowtell, L.T. Elliott, S.M. Smith, B.C. Tendler, K.L. Miller, Phenotypic and genetic associations of quantitative magnetic susceptibility in UK biobank brain imaging, Nature Neurosci. 25 (6) (2022) 818–831, http://dx.doi.org/10.1038/s41593-022-01074-w.

[45] T. Liu, P. Spincemaille, L. de Rochefort, B. Kressler, Y. Wang, Calculation of susceptibility through multiple orientation sampling (COSMOS): A method for conditioning the inverse problem from measured magnetic field map to susceptibility source image in MRI, Magn. Reson. Med. 61 (1) (2009) 196–204, http://dx.doi.org/10.1002/mrm.21828.

[46] E.M. Haacke, Y. Xu, Y.-C.N. Cheng, J.R. Reichenbach, Susceptibility weighted imaging (SWI), Magn. Reson. Med. 52 (3) (2004) 612–618, http://dx.doi.org/10.1002/mrm.20198.

[47] C. Liu, Susceptibility tensor imaging, Magn. Reson. Med. 63 (6) (2010) 1471–1477, http://dx.doi.org/10.1002/mrm.22482.

[48] G.A. Álvarez, N. Shemesh, L. Frydman, Diffusion-assisted selective dynamical recoupling: A new approach to measure background gradients in magnetic resonance, J. Chem. Phys. 140 (8) (2014) 084205, http://dx.doi.org/10.1063/1.4865335.

[49] G.A. Álvarez, N. Shemesh, L. Frydman, Internal gradient distributions: A susceptibility-derived tensor delivering morphologies by magnetic resonance, Sci. Rep. 7 (2017) 3311, http://dx.doi.org/10.1038/s41598-017-03277-9.

[50] A.D. Sandgaard, V.G. Kiselev, N. Shemesh, S.N. Jespersen, Incorporating white matter microstructure in the estimation of magnetic susceptibility in ex-vivo mouse brain, 2022, http://dx.doi.org/10.48550/ARXIV.2208.02594.

[51] R. Karlicek, I. Lowe, A modified pulsed gradient technique for measuring diffusion in the presence of large background gradients, J. Magn. Reson. 37 (1) (1980) 75–91, http://dx.doi.org/10.1016/0022-2364(80)90095-5.

[52] M.D. Does, J. Zhong, J.C. Gore, In vivo measurement of ADC change due to intravascular susceptibility variation, Magn. Reson. Med. 41 (2) (1999) 236–240, http://dx.doi.org/10.1002/(sici)1522-2594(199902)41:2<236::aid-mrm4>3.0.co;2-3.

[53] A. Pampel, T.H. Jochimsen, H.E. Möller, BOLD background gradient contributions in diffusion-weighted fMRI-comparison of spin-echo and twice-refocused spin-echo sequences, NMR Biomed. 23 (6) (2010) 610–618, http://dx.doi.org/10.1002/nbm.1502.

[54] D.S. Novikov, M. Reisert, V.G. Kiselev, Effects of mesoscopic susceptibility and transverse relaxation on diffusion NMR, J. Magn. Reson. 293 (2018) 134–144, http://dx.doi.org/10.1016/j.jmr.2018.06.007.

[55] G. Costantini, S. Capuani, F.A. Farrelly, A. Taloni, Nuclear magnetic resonance signal decay in the presence of a background gradient: Normal and anomalous diffusion, J. Chem. Phys. 158 (17) (2023) 174106, http://dx.doi.org/10.1063/5.0148175.

[56] Y.-Q. Song, S. Ryu, P.N. Sen, Determining multiple length scales in rocks, Nature 406 (6792) (2000) 178–181, http://dx.doi.org/10.1038/35018057.

[57] Q. Chen, M.K. Gingras, B.J. Balcom, A magnetic resonance study of pore filling processes during spontaneous imbibition in berea sandstone, J. Chem. Phys. 119 (18) (2003) 9609–9616, http://dx.doi.org/10.1063/1.1615757.

[58] J.-F. Kuntz, G. Trausch, P. Palmas, P. Mutzenhardt, D. Canet, Diffusive diffraction phenomenon in a porous polymer material observed by NMR using radio-frequency field gradients, J. Chem. Phys. 126 (13) (2007) 134904, http://dx.doi.org/10.1063/1.2713379.

[59] H. Liu, M.N. d'Eurydice, S. Obruchkov, P. Galvosas, Determining pore length scales and pore surface relaxivity of rock cores by internal magnetic fields modulation at 2 MHz NMR, J. Magn. Reson. 246 (2014) 110–118, http://dx.doi.org/10.1016/j.jmr.2014.07.005.

[60] Y. Zhang, L. Xiao, G. Liao, B. Blümich, Direct correlation of internal gradients and pore size distributions with low field NMR, J. Magn. Reson. 267 (2016) 37–42, http://dx.doi.org/10.1016/j.jmr.2016.04.009.

[61] S. Han, Y. Song, F. Cho, S. Ryu, G. Cho, Y.-Q. Song, H. Cho, Magnetic field anisotropy based MR tractography, J. Magn. Reson. 212 (2) (2011) 386–393, http://dx.doi.org/10.1016/j.jmr.2011.07.021.

[62] S. Winther, H. Lundell, J. Rafael-Patiño, M. Andersson, J.-P. Thiran, T.B. Dyrby, Susceptibility-induced internal gradients reveal axon morphology and cause anisotropic effects in the dMRI signal, 2023, http://dx.doi.org/10.1101/2023.05.01.538981,

[63] W.C. Chen, S. Foxley, K.L. Miller, Detecting microstructural properties of white matter based on compartmentalization of magnetic susceptibility, NeuroImage 70 (2013) 1–9, http://dx.doi.org/10.1016/j.neuroimage.2012.12.032.

[64] T. Xu, S. Foxley, M. Kleinnijenhuis, W.C. Chen, K.L. Miller, The effect of realistic geometries on the susceptibility-weighted MR signal in white matter, Magn. Reson. Med. 79 (1) (2017) 489–500, http://dx.doi.org/10.1002/mrm.26689.

[65] J.E. Fajardo, G.A. Álvarez, Internal gradient distribution tensors of white matter tracts models, Proc. Intl. Soc. Mag. Reson. Med. 13 (29) (2021) 1716.

[66] H. Cho, S. Ryu, J. Ackerman, Y.-Q. Song, Visualization of inhomogeneous local magnetic field gradient due to susceptibility contrast, J. Magn. Reson. 198 (1) (2009) 88–93, http://dx.doi.org/10.1016/j.jmr.2009.01.024.

[67] P.T. Callaghan, J. Stepišnik, Frequency-domain analysis of spin motion using modulated-gradient NMR, J. Magn. Reson. A 117 (1) (1995) 118, http://dx.doi.org/10.1006/jmra.1995.9959.

[68] E.L. Hahn, Spin echoes, Phys. Rev. 80 (1950) 580, http://dx.doi.org/10.1103/PhysRev.80.580.

[69] H.Y. Carr, E.M. Purcell, Effects of diffusion on free precession in nuclear magnetic resonance experiments, Phys. Rev. 94 (1954) 630, http://dx.doi.org/10.1103/PhysRev.94.630.

[70] S. Meiboom, D. Gill, Modified spin-echo method for measuring nuclear relaxation times, Rev. Sci. Instrum. 29 (8) (1958) 688, http://dx.doi.org/10.1063/1.1716296, arXiv:https://doi.org/10.1063/1.1716296.

[71] E.O. Stejskal, J.E. Tanner, Spin diffusion measurements: Spin echoes in the presence of a time-dependent field gradient, J. Chem. Phys. 42 (1) (1965) 288, http://dx.doi.org/10.1063/1.1695690.

[72] D. Le Bihan, Looking into the functional architecture of the brain with diffusion MRI, Nat. Rev. Neurosci. 4 (6) (2003) 469, http://dx.doi.org/10.1038/nrn1119.
[73] D.K. Jones, Diffusion MRI, Oxford University Press, 2010.
[74] N. Shemesh, G.A. Álvarez, L. Frydman, Measuring small compartment dimensions by probing diffusion dynamics via non-uniform oscillating-gradient spin-echo (NOGSE) NMR, J. Magn. Reson. 237 (2013) 49, http://dx.doi.org/10.1016/j.jmr.2013.09.009.
[75] C.H. Neuman, Spin echo of spins diffusing in a bounded medium, J. Chem. Phys. 60 (11) (1974) 4508–4511, http://dx.doi.org/10.1063/1.1680931.
[76] J. Stepišnik, Validity limits of Gaussian approximation in cumulant expansion for diffusion attenuation of spin echo, Phys. B 270 (1) (1999) 110, http://dx.doi.org/10.1016/S0921-4526(99)00160-X.
[77] R. Kubo, Generalized cumulant expansion method, J. Phys. Soc. Japan 17 (7) (1962) 1100–1120, http://dx.doi.org/10.1143/jpsj.17.1100.
[78] N.V. Kampen, Stochastic Processes in Physics and Chemistry, Elsevier, 2007, pp. 52–72, http://dx.doi.org/10.1016/b978-044452965-7/50006-4.
[79] J. Stepišnik, S. Lasič, A. Mohorič, I. Serša, A. Sepe, Spectral characterization of diffusion in porous media by the modulated gradient spin echo with CPMG sequence, J. Magn. Reson. 182 (2) (2006) 195, http://dx.doi.org/10.1016/j.jmr.2006.06.023.
[80] S. Lasič, J. Stepišnik, A. Mohoric, Displacement power spectrum measurement by CPMG in constant gradient, J. Magn. Reson. 182 (2006) 208, http://dx.doi.org/10.1016/j.jmr.2006.06.030.
[81] J.R. Klauder, P.W. Anderson, Spectral diffusion decay in spin resonance experiments, Phys. Rev. 125 (3) (1962) 912, http://dx.doi.org/10.1103/PhysRev.125.912.
[82] G.E. Uhlenbeck, L.S. Ornstein, On the theory of the Brownian motion, Phys. Rev. 36 (5) (1930) 823–841, http://dx.doi.org/10.1103/physrev.36.823.
[83] M. Kuffer, A. Zwick, G.A. Álvarez, Path integral framework for characterizing and controlling decoherence induced by nonstationary environments on a quantum probe, PRX Quant. 3 (2022) 020321, http://dx.doi.org/10.1103/PRXQuantum.3.020321.
[84] R.C. Wayne, R.M. Cotts, Nuclear-magnetic-resonance study of self-diffusion in a bounded medium, Phys. Rev. 151 (1966) 264–272, http://dx.doi.org/10.1103/PhysRev.151.264.
[85] B. Robertson, Spin-echo decay of spins diffusing in a bounded region, Phys. Rev. 151 (1966) 273–277, http://dx.doi.org/10.1103/PhysRev.151.273.
[86] J. Stepišnik, Time-dependent self-diffusion by NMR spin-echo, Phys. B 183 (4) (1993) 343, http://dx.doi.org/10.1016/0921-4526(93)90124-O.
[87] G.A. Álvarez, N. Shemesh, L. Frydman, Coherent dynamical recoupling of diffusion-driven decoherence in magnetic resonance, Phys. Rev. Lett. 111 (2013) 080404, http://dx.doi.org/10.1103/PhysRevLett.111.080404.
[88] A. Zwick, D. Suter, G. Kurizki, G.A. Álvarez, Precision limits of tissue microstructure characterization by magnetic resonance imaging, Phys. Rev. Appl. 14 (2020) 024088, http://dx.doi.org/10.1103/PhysRevApplied.14.024088.
[89] P. Vatiwutipong, N. Phewchean, Alternative way to derive the distribution of the multivariate Ornstein–Uhlenbeck process, Adv. Differential Equations 2019 (2019) 276, http://dx.doi.org/10.1186/s13662-019-2214-1.
[90] E. Caruyer, C. Lenglet, G. Sapiro, R. Deriche, Design of multishell sampling schemes with uniform coverage in diffusion MRI, Magn. Reson. Med. 69 (6) (2013) 1534–1540, http://dx.doi.org/10.1002/mrm.24736.
[91] R.V. Mulkern, H. Gudbjartsson, C.-F. Westin, H.P. Zengingonul, W. Gartner, C.R.G. Guttmann, R.L. Robertson, W. Kyriakos, R. Schwartz, D. Holtzman, F.A. Jolesz, S.E. Maier, Multi-component apparent diffusion coefficients in human brain, NMR Biomed. 12 (1) (1999) 51–62, http://dx.doi.org/10.1002/(sici)1099-1492(199902)12:1<51::aid-nbm546>3.0.co;2-e.
[92] S.E. Maier, P. Bogner, G. Bajzik, H. Mamata, Y. Mamata, I. Repa, F.A. Jolesz, R.V. Mulkern, Normal brain and brain tumor: Multicomponent apparent diffusion coefficient line scan imaging, Radiology 219 (3) (2001) 842–849, http://dx.doi.org/10.1148/radiology.219.3.r01jn02842.
[93] R. Sener, Diffusion MRI: apparent diffusion coefficient (ADC) values in the normal brain and a classification of brain disorders based on ADC values, Comput. Med. Imaging Graph. 25 (4) (2001) 299–326, http://dx.doi.org/10.1016/s0895-6111(00)00083-5.
[94] P. Tofts, D. Lloyd, C. Clark, G. Barker, G. Parker, P. McConville, C. Baldock, J. Pope, Test liquids for quantitative MRI measurements of self-diffusion coefficient in vivo, Magn. Reson. Med. 43 (3) (2000) 368–374, http://dx.doi.org/10.1002/(sici)1522-2594(200003)43:3<368::aid-mrm8>3.0.co;2-b.
[95] F.S. Mikelberg, S.M. Drance, M. Schulzer, H.M. Yidegiligne, M.M. Weis, The normal human optic nerve: Axon count and axon diameter distribution, Ophthalmology 96 (9) (1989) 1325–1328, http://dx.doi.org/10.1016/S0161-6420(89)32718-7.
[96] D. Barazany, P.J. Basser, Y. Assaf, In vivo measurement of axon diameter distribution in the corpus callosum of rat brain, Brain 132 (5) (2009) 1210–1220, http://dx.doi.org/10.1093/brain/awp042.
[97] S.Y. Huang, Q. Tian, Q. Fan, Q. Fan, T. Witzel, B. Wichtmann, J.A. McNab, J. Daniel Bireley, N. Machado, E.C. Klawiter, C. Mekkaoui, L.L. Wald, A. Nummenmaa, High-gradient diffusion MRI reveals distinct estimates of axon diameter index within different white matter tracts in the in vivo human brain, Brain Struct. Funct. 225 (4) (2020) 1277–1291, http://dx.doi.org/10.1007/s00429-019-01961-2.
[98] T. Mingasson, T. Duval, N. Stikov, J. Cohen-Adad, AxonPacking: An open-source software to simulate arrangements of axons in white matter, Front. Neuroinf. 11 (5) (2017) 1–12, http://dx.doi.org/10.3389/fninf.2017.00005.
[99] A.P. Pathak, B.D. Ward, K.M. Schmainda, A novel technique for modeling susceptibility-based contrast mechanisms for arbitrary microvascular geometries: The finite perturber method, NeuroImage 40 (3) (2008) 1130–1143, http://dx.doi.org/10.1016/j.neuroimage.2008.01.022.
[100] D. Bailes, I. Young, D. Thomas, K. Straughan, G. Bydder, R. Steiner, NMR imaging of the brain using spin-echo sequences, Clin. Radiol. 33 (4) (1982) 395–414, http://dx.doi.org/10.1016/s0009-9260(82)80307-3.
[101] B.A. Holland, D.K. Haas, D. Norman, M. Brant-Zawadzki, T.H. Newton, MRI of normal brain maturation., Am. J. Neuroradiol. 7 (2) (1986) 201–208.
[102] J.P. Wansapura, S.K. Holland, R.S. Dunn, W.S. Ball, NMR relaxation times in the human brain at 3.0 tesla, J. Magn. Reson. Imaging 9 (4) (1999) 531–538, http://dx.doi.org/10.1002/(sici)1522-2586(199904)9:4<531::aid-jmri4>3.0.co;2-l.
[103] Y.-Q. Song, Using internal magnetic fields to obtain pore size distributions of porous media, Concepts Magn. Reson. 18A (2) (2003) 97–110, http://dx.doi.org/10.1002/cmr.a.10072.
[104] V.G. Kiselev, K.A. Il'yasov, Is the "biexponential diffusion" biexponential? Magn. Reson. Med. 57 (3) (2007) 464, http://dx.doi.org/10.1002/mrm.21164.